# Advanced Control and Stability Enhancement of Grid-Connected Voltage-Source Inverter with LCL-Filter

Xin, Zhen

*Publication date:*
2017

*Document Version*
Publisher's PDF, also known as Version of record

# ADVANCED CONTROL AND STABILITY ENHANCEMENT OF GRID-CONNECTED VOLTAGE-SOURCE INVERTER WITH LCL-FILTER

**BY**
**ZHEN XIN**

DISSERTATION SUBMITTED 2017

AALBORG UNIVERSITY
DENMARK

# ADVANCED CONTROL AND STABILITY ENHANCEMENT OF GRID-CONNECTED VOLTAGE-SOURCE INVERTER WITH LCL-FILTER

**PH.D. THESIS**

by

Zhen Xin

AALBORG UNIVERSITY
DENMARK

Dissertation submitted 2017

.

Dissertation submitted: March 21, 2017

PhD supervisor: Prof. Frede Blaabjerg,
Aalborg University

Assistant PhD supervisor: Dr. Xiongfei Wang,
Aalborg University

PhD committee: Remus Teodorescu (Chairman)
Aalborg University

Josep Pou, Co-Director
Nanyang Technological University (NTU)

Vassilios Georgios AGELIDIS
DTU

PhD Series: Faculty of Engineering and Science, Aalborg University

ISSN (online): 2446-1636
ISBN (online): 978-87-7112-927-4

Published by:
Aalborg University Press
Skjernvej 4A, 2nd floor
DK – 9220 Aalborg Ø
Phone: +45 99407140
aauf@forlag.aau.dk
forlag.aau.dk



Printed in Denmark by Rosendahls, 2017

# CV

Zhen Xin was born in Shandong Province, China. He received the B.S. and M.S. degrees from College of Information and Control Engineering, China University of Petroleum, Qingdao, China, in 2011 and 2014, respectively. He was a visiting scholar with University of Padova, Padova, Italy, from May to August in 2016. He is currently working toward the Ph.D. degree at Department of Energy Technology, Aalborg University, Aalborg, Denmark. His research interests include stability analysis and control of power-electronics based power systems, harmonic identification and mitigation in power converters, motor drives, and high-bandwidth current sensors. Zhen Xin is a Student Member of the Institute of Electrical and Electronics Engineers (IEEE), the IEEE Power Electronics Society, and the IEEE Industry Applications Society. He is also a reviewer for various top journals and conferences like IEEE Transactions on Power Electronics, IEEE Transactions on Industry Applications, IET Power Electronics, IEEE ECCE and APEC conferences.

# ENGLISH SUMMARY

Power converters have been widely used in renewable energy generation systems, whose high penetration into the grid is changing the characteristic of the traditional power system and imposing new challenges. Among different topologies of power converters, the LCL-filtered Voltage-Source Inverter (VSI) is the most commonly used interface between the renewable energy generation system and the power grid. However, the LCL-filtered VSI may introduce resonance into the system which reduces the power quality and more seriously, triggers system instability. Moreover, compared with the simple L-filtered VSI, the LCL-filtered VSI is sensitive to low-order harmonics, due to its small impedance at low frequencies as seen from both the inverter-side and the grid-side.

On one hand, to enhance the system stability, the resonance of the LCL-filter must be damped properly using either active or passive damping techniques. Although the principle of the damping function is simple, its implementation may cause more losses, increased cost and design complexity of the system. Recent publications have researched the fundamental mechanism and the parameter design of active damping, but there is limited discussion about its practical implementation issues and stability enhancement techniques. On the other hand, to enhance the harmonic attenuation performance of the LCL-filtered VSI, diverse control methods have been developed. However, there is still not a cost-effective solution for harmonic suppression of the system with inverter-side current control in which the grid-current harmonics can freely flow into the capacitor without control. Moreover, most grid standards work on the premise of a harmonic-free grid, which is inconsistent with the real cases. It has been reported that an IEEE-1547-compliant PV inverter produces over 20 % total demand distortion under 3 % grid voltage distortion. Harmonic attenuation of the grid-connected VSI under distorted grid voltage is still an open research.

This thesis has developed corresponding solutions to cope with the aforementioned issues. The first contribution of this thesis lays on the development of two advanced digital differentiators which can ensure a cost-effective implementation of the active damping. Then, a robust damping gain is derived for the grid-current control system and a time-delay compensation technique is developed to further enhance the system stability. The knowledge obtained in the former is then used to develop a simple harmonic mitigation strategy for the LCL-filtered VSI with inverter-side current control. Finally, an improved Quadrature-Signal Generator (QSG) is proposed for grid synchronization, which inherits the simplicity of the second-order generalized integrator based QSG while still has an enhanced harmonic attenuation performance.

All the developments presented in this thesis have been validated by simulation and/or experimental results. These contributions have been published in 8 journal papers and 7 conference papers.

# DANSK RESUME

Energiomformere er I udvidet grad blevet brugt I vedvarende energi generation systemer, hvis høje markedsindtrængen ændre karakteristikken af det konventionelle energisystem, og skaber store tekniske udfordringer. Blandt forskellige topologier om energi omformere, er LCL-filreret Voltage-Source Inverter (VSI) den mest almindeligt brugte grænseflade mellem vedvarende energiudvindingssystemer og højspændingsnettet. Med hensyn til LCL-filtreret VSI, bliver to udfordringer gentagende gange indrapporteret, som er relateret til systemets stabilitet og energikvalitet.

Særligt LCL-filteret kan skabe resonans, hvilket skal dæmpes på forsvarlig vis, enten ved brug af aktive eller passive dæmpningsstrategier, for at sikre systemets stabilitet. Selvom principperne af dæmpningsfunktionen er simple og lige til, kan implementeringen heraf forårsage flere tab, forøgede omkostninger og/eller designkompleksitet af vekselrettersystemet. På trods af den store mængde af litteratur omhandlende stabilitetsanalyse og dæmpningsdesign af LCL-filtreret VSI, er der stadig begrænset analyse om de praktiske implementeringsudfordringer og teknikker for stabilitetstiltag af den aktive dæmpningskontrol. En anden udfordring skabt af LCL-filtreret VSI er den ringe energi, apparater producerer under forvrænget netværksspænding. Det er nyligt anerkendt at lav induktans af LCL-filteret potentielt skaber kraftige strømforvrængninger i højspændingsnettet under bare lidt forvrænget spænding i højspændingsnettet. Især hidtil, for den kommercielt fortrukne styringsplan (vekselretter-sidestrømskontrol), er der stadigvæk ikke nogen effektiv løsning i eksisterende litteratur.

Dette speciale udviklede tilsvarende løsninger for at tage højde for de førnævnte problemstillinger. Det første bidrag fra dette speciale ligger i udviklingen af to avancerede digitale differentiatorer, som hjælper til at forstå en omkostnings-effektiv implementering af den aktive dæmpnings funktion. Det andet bidrag er den robuste dæmpningsforøgelse udledt af højspændingsnettets strømkontrolsystem, og en kompensationsteknik for tidsforsinkelse udviklet for at forbedre stabiliteten af kontrolsystemet. Den forefundne viden i de to bidrag bliver herefter brugt til at udvikle en simpel men effektiv harmonikontrolstrategi for det LCL-filrerede VSI, ved brug af en vekselretter-strømnings feedbackkontrol. Den forslåede kontrolordning er ækvivalent med et system der anvender en proportionalkontrol til vekselretter-strømningen og en resonansstyreenhed til strømmen i højspændingsnettet, hvis parameterdesign kan være ligeså simple som de typiske enkelt-loop strømningskontrolsystemer. Endeligt, bliver en forbedret kvadreringssignalgenerator (QSG) forslået, hvilket kan blive brugt til højspændingsnetssynkronisering. Den forslåede QSG arver simpliciteten af den grundlæggende SOGI-QSG, men har en forbedret filtreringsydeevne, hvilket

medfører, en mere fremragende ydeevne i tilfælde af forvrængninger højspændingsnettet.

Alle de præsenterede udviklinger i dette speciale er blevet valideret af simulations- og/eller eksperimentale resultater. Disse bidrag er blevet publiceret i 8 tidsskriftsartikler og 7 konferenceindlæg.

# ACKNOWLEDGEMENTS

This research has received funding from the China Scholarship Council and the European Research Council (ERC) under the European Unions Seventh Framework Program (FP7/2007-2013)/ERC Grant 321149-Harmony. Their supports are greatly acknowledged. I would also like to show acknowledgements to Aalborg University, and Otto Mønsteds Fond, who provided financial and/or environmental supports to my research. Sincere thanks go to Mr. Yun Zhang from the Embassy of The People's Republic of China in The Kingdom of Denmark for his enthusiastic help.

My deepest gratitude goes first and foremost to Prof. Frede Blaabjerg, my supervisor, for his patient guidance, enthusiasm, and constant encouragement. He respects my interests and provides instructive advices and valuable opportunities for my academic research. I feel grateful to have been given the opportunity to work with such an outstanding professor. Without his supervision and persistent help, this thesis would have never been possible.

Also, I would like to express my heartfelt gratitude to Prof. Poh Chiang Loh, who plays the role of a teacher and also a friend in my life. His encouragement helped me to gain confidence and his guidance prompted me to make feasible plans.

High tribute shall be paid to Prof. Paolo Mattavelli for his kindness during my stay at University of Padova, where I benefited a lot from the discussions with him.

Many thanks go to Prof. Rende Zhao from China University of Petroleum, for his comments and discussions during my Ph.D. period.

I want to thank my thesis committee: Prof. Remus Teodorescu, Prof. Josep Pou, and Prof. Vassilios Georgios AGELIDIS for providing their valuable time, advice and support along the way.

My thanks go to Dr. Xiongfei Wang, the past and the present members of Harmony group. Thanks for all the assistance I have received from my colleagues.

Special thanks should go to Dr. Huai Wang, Dr. Yongheng Yang, Dr. Yi Tang, Dr. Xiaohui Qu, Dr. Dao Zhou, Dr. Pooya Davari, and Dr. Hao Yi, for their encouragement and suggestions to my research.

Especially, I take this opportunity to thank Dr. Yanbo Wang and Dr. Zi'an Qin for their brother-like care and spiritual support over the past 2 years. I want to thank my friend Minghui Lu for his accompany and support, who was with me all the way on the journey of my Ph.D. Many thanks go to my friends Zhen Zhang, Dan Wu,

Changwoo Yoon, Dapeng Lu, Ronggang Ni, Qing Zeng, Haofeng Bai, Chong Zhang, and Min Huang. They made my life in Aalborg more enjoyable. Many thanks go to all local and external colleagues from the Department of Energy Technology and I sincerely appreciate the friendly working environment at the department.

I want to express my sincere gratitude to my parents, sister and my wife for their concerns and understanding. Without their unconditional love and support, I would nowhere close to where I am today. To them, I dedicate this thesis.

Zhen Xin

March 21, 2017
Aalborg Øst, Denmark

# TABLE OF CONTENTS

# TABLE OF FIGURES

# CHAPTER 1. INTRODUCTION

## 1.1. BACKGROUND

From 2015 to 2040, the global electricity demand is predicted to rise by 60 %, which, inevitably, will continue to drive the greenhouse gas emissions higher that have already risen by 50 % from 1990 to 2014 [1]. To address the environmental issues, energy production is changing from conventional fossil fuels to renewable energies, such as wind, solar and biofuels which are expected to be more than tripled from 2014 to 2040 [2]. At the same time, the grid-connected inverters, which are the interfaces between the power generators (wind generator, solar panel, and hydro-electric generator) and the grid, are becoming more and more popular in the power system, making the conventional power system more power-electronic based. However, it has gradually found that the high penetration of power converters changes the characteristic of the power system and imposes new challenges to the end-consumers and the distributed system operators in terms of safety operation and power quality [3] [4]:

- The capacitance in filters (e.g. LCL-filter) and power factor correction units, as well as the parasitic capacitance in power lines, combined with the inductances, may introduce resonances which threat the safe operation of the power system. Moreover, the interactions among the control systems of different power inverters are also susceptible to the generation of harmonic oscillations.
- The grid-connected inverter, if not controlled properly, may generate low harmonic impedance which can produce severe grid-current distortion even when the grid voltage is slightly distorted. This problem can be even more serious with the increased use of nonlinear loads in the power system.

Therefore, it is essential to develop necessary control strategies for grid-connected inverters in order to cost-effectively enhance the stability and the power quality of the renewable energy generation systems and then to enable a further increase of the contribution of the renewable energies to the global electricity demand.

Among different power conversion topologies, the Voltage-Source Inverter (VSI) is usually applied for the renewable energy sources to regulate the power injected to the grid [5]–[8]. To avoid the adverse effects of power converters, low-distortion output current is required by grid standards (e.g. IEEE 1547-2003). Therefore, series line filters are used as the interface between the VSI and the grid in order to attenuate the high-frequency switching harmonics generated by the Pulse Width Modulation (PWM) process. Generally, this filter can be either an L filter or an LCL filter, while the latter is much preferred in practice owning to its strong filtering

performance obtained with reduced inductance and cost [9]–[11]. Figure 1-1 shows the typical structure of a three-phase VSI system which is connected to the grid through an LCL-filter. The line filter contains inverter-side inductor $L_1$, capacitor $C$, and grid-side inductor $L_2$. Generally, either the grid-side current $i_2$ or the inverter-side current $i_1$ is controlled in order to regulate the power injected to the grid. Besides, the grid voltage $v_g$ or the capacitor voltage $v_C$ is measured for grid synchronization.

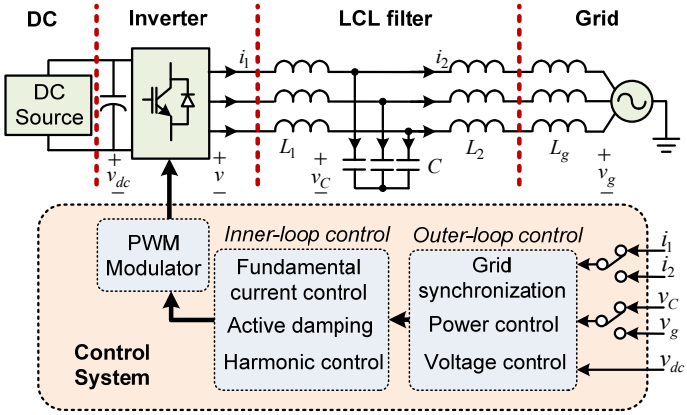


*Figure 1-1 Typical structure of the three-phase Voltage-Source Inverter (VSI) system.*

### 1.1.1. LCL-FILTER

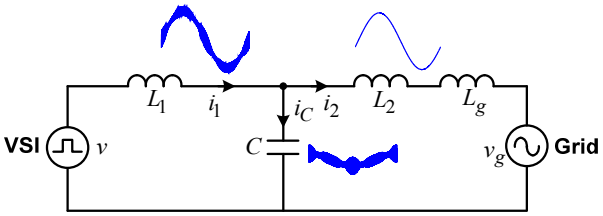


*Figure 1-2 Single-phase equivalent circuit of the grid-connected VSI with LCL-filter.*

The single-phase equivalent circuit of the LCL-filtered VSI is shown in Figure 1-2. Regarding the design of the LCL-filter, typically, the inverter-side inductance should be designed to limit the ripple current within 15 % ~ 40 % of the rated current for safe operation [11]–[14]. As for the capacitor, small capacitance will lead to large inductance for the same attenuation performance, making the LCL-filter lose its advantage. On the other hand, a large capacitance can cause large reactive power provided by the inverter, which leads to low efficiency of the VSI system [13]. In practice, the capacitor current should be restricted to 5 % ~15 % of the rated current [14]. The grid-side inductance should ensure that the switching harmonics in the

grid current can finally be attenuated below the limits required by grid standard. However, with the increased penetration of power converters in the power system, design of the LCL-filter should also consider the robustness of the system against grid-impedance variation and the immunity of the system to grid-voltage distortion.

### 1.1.2. CURRENT REGULATION

To regulate the output power of the VSI, both the grid-side current and the inverter-side current can be controlled. The control system can be implemented in either synchronous frame using a Proportional Integral (PI) controller or stationary frame using a Proportional Resonant (PR) controller. As for the Grid-Current Feedback (GCF) control, the grid current is regulated directly, which means that the low-order current harmonics injected to the grid can be controlled using Harmonic Controllers (HCs). However, its main disadvantage is extra cost for grid-current measurement. This drawback can be well overcome by the Inverter-Current Feedback (ICF) control, since current sensors have been installed in inverter-side for overcurrent protection and thus, extra sensors for the control loop can be avoided. However, the main disadvantage of the ICF scheme is its indirect regulation of the injected grid current, which limits the harmonic controllability. Despite the simplicity of the GCF and ICF control, development of the appropriate control schemes, which are able to overcome the drawbacks of these two schemes and, at the same time, retain their advantages, has important practical value.

### 1.1.3. ACTIVE DAMPING

The main issue of the LCL-filter is that it may introduce resonances into the system, which reduce the power quality and threat the system stability. Generally, the resonances can be damped passively by adding resistors in the LCL-filter network. However, the passive damping strategies usually generate high losses and reduce the efficiency of the system [15]. Therefore, active damping is suggested in [15]–[19], whose basic working principle is to mimic a resistor through feeding back some variables in the control loop. The variables can be the capacitor current $i_C$ [18], [20], [21], the capacitor voltage $v_C$ [17], [19], [22], and the grid current $i_2$ [23], [24]. Although there are plenty of papers published about active damping, its practical implementation issues and the stability enhancement techniques are still not well investigated.

### 1.1.4. HARMONIC CONTROL

Generally, in order to avoid the adverse effects of the power converters on power quality, low-distortion output current is required by the grid standards such as IEEE 1547-2003 which specifies the limits of both low- and high-frequency harmonics [25]. However, most grid standards work on the premise of a harmonic-free grid, which is inconsistent with the real case [25], [26]. It has been reported that an IEEE-

1547-compliant PV inverter produces over 20 % Total Demand Distortion (TDD) under 3 % grid voltage distortion, which, in comparison, has only 0.66 % TDD under an ideal grid condition [26]. As mentioned previously, this issue is especially tough for the ICF control system, since the grid-current harmonics can freely flow into the filter capacitor without control. Due to the loss of harmonic information, traditional HCs are helpless for the ICF control system to mitigate the grid-side current distortion. Although this issue can be solved by the grid-voltage feedforward scheme [27], the required second-order differentiator may cause noise amplification. Therefore, harmonic attenuation of the grid-connected inverters under distorted grid voltage is still an open research challenge [28]–[30].

### 1.1.5. GRID SYNCHRONIZATION

Grid synchronization provides the phase and/or frequency information of the grid-voltage for the control system, which should be fast and accurate in order to ensure a high-performance operation of the grid-connected VSI especially under adverse grid condition. The synchronization function can be implemented by either frequency-domain methods (e.g. discrete Fourier transform) or time-domain methods (e.g. Phase-Locked Loop, (PLL)) [31]. Among these methods, the PLL is widely used in power converter applications. For single-phase-system usage, the main difference of the PLL-based methods is the implementation of the phase detector which is usually built by a Quadrature Signal Generator (QSG). The widely reported QSGs in literature are $T/4$ delay technique, Hilbert transform, inverse-park transform, and adaptive filters (e.g. enhanced PLL and SOGI-QSG). Among these techniques, the SOGI-QSG is a promising candidate since it is able to track the input exactly [32]. Moreover, for three-phase systems, the SOGI-QSG is very flexible to be applied for extracting the positive and negative components from the grid voltage, which is useful especially under greatly unbalanced grid conditions [33]. However, the basic SOGI-QSG is sensitive to the input harmonics and dc offset [34], [35]. In order to enhance its performance, it is necessary to develop some advanced structures.

## 1.2. RESEARCH OBJECTIVES

To address the aforementioned challenges, this thesis has the following objectives:

*1. How to implement active damping cost-effectively without extra current sensors?*

The active damping implemented by feeding back capacitor current is a commonly used approach, which, however, needs additional sensors to measure the capacitor current. Economically, the capacitor voltage can be used to calculate the capacitor current, if it has already been used for grid synchronization. However, the differentiator, when discretized, suffers from noise-amplification and phase-error issues. This thesis will investigate the impacts of traditional discretization methods on system stability and explore improved digital differentiators to solve the issues.

*2. How to enhance the system stability under grid impedance variation?*

Active damping can damp the LCL-filter resonance and ensure the system stability. However, grid impedance variation may reduce the system stable margin and even cause system instability. This thesis will develop suitable control strategy to enhance the system stability.

*3. Why is the LCL-filtered VSI sensitive to the low-order grid-voltage harmonics, and how to improve the harmonic control performance of the ICF-controlled VSI?*

This thesis will explore the root causes of the harmonic issues of the LCL-filtered VSI, especially when the ICF control scheme is applied. Limitations of the traditional solutions will be analyzed and solutions will be explored.

*4. How to improve the harmonic-attenuation and dc-rejection performance of the SOGI-QSG and, at the same time, retain its simplicity in parameter design and implementation?*

Harmonics and dc offsets can cause errors at the output of SOGI-QSG, which should be suppressed. This thesis will develop improved algorithm to reduce these effects.

## 1.3. LIMITATIONS

This thesis mainly concentrates on the stability analysis of the inner current control loop, while the impacts of the outer loops, such as the power control loop, are not studied in the thesis. Moreover, although the proposed methods in the thesis are appropriate to many renewable energy generation applications, they have not been tested under a real mission profile. Further, the parasitic resistances of the filters and the non-linear factors in the system (e.g. deadtime effect, modulation schemes and the saturation of the inductors) also have impacts on the system stability, which are not investigated in the thesis.

## 1.4. THESIS OUTLINE

This thesis is written as ***a collection of articles***, which mainly contains two parts. The first part is the thesis report and the second part is the attached published papers. The thesis report contains 6 chapters which are introduced as follows:

*Chapter 1* gives the background, objectives, and list of publications.

*Chapter 2* addresses the practical implementation issue of the active damping control. It begins by modeling the single-loop GCF and ICF control systems, based on which, the stable regions and unstable regions of these two systems are identified. Next, the practical implementation issues of active damping are analyzed. To solve

the problem, two differentiators based on the non-ideal Generalized Integrator (GI) and the Second-Order Generalized Integrator (SOGI) are proposed.

*Chapter 3* focuses on the stability enhancement of the current control system using time-delay compensation strategy. To begin with, an optimized inner-loop damping gain is determined for the dual-loop GCF scheme with active damping, which is able to fix the stable region of the system always below a critical frequency, regardless of the variation of the grid impedance and LCL-filter parameters. Finally, an improved time-delay compensation method is presented to enhance the system stability.

*Chapter 4* begins by investigating the sensitivity of the ICF-controlled VSI to the grid-voltage harmonics. The limitations of the traditional harmonic suppression strategies, such as harmonic controllers and grid-voltage feedforward schemes, are identified. Finally, a simple and effective control scheme is proposed to overcome the problems.

*Chapter 5* first presents a comprehensive review of the SOGI-based filters from a first-order system and a circuit perspective, based on which, the principle of the SOGI-based filters are intuitively understood. Further, two advanced SOGI-QSGs are proposed. The first one is a fourth-order system, which has enhanced filtering performance for both low-frequency and high-frequency components. The second one is a second-order system, which has similar performance to the basic SOGI-QSG but it can realize parameter design based on desired transient performance.

*Chapter 6* gives the summary and future works of the thesis.

## 1.5. LIST OF PUBLICATIONS

A list of journal papers related to the thesis, which have been published or submitted till now, is given as follows:

**J1.** **Z. Xin**, X. Wang, P. C. Loh, and F. Blaabjerg, "Realization of digital differentiator using generalized integrator for power converters," *IEEE Trans. Power Electron*., vol. 30, no. 12, pp. 6520–6523, Dec. 2015.

**J2.** **Z. Xin**, P. C. Loh, X. Wang, F. Blaabjerg, and Y. Tang, "Highly accurate derivatives for LCL-Filtered grid converter with capacitor voltage active damping," *IEEE Trans. Power Electron.*, vol. 31, no. 5, pp. 3612–3625, May 2016.

**J3.** **Z. Xin**, X. Wang, Z. Qin, M. Lu, P. C. Loh, and F. Blaabjerg, "An improved second-order generalized integrator based quadrature signal generator," *IEEE Trans. Power Electron*., vol. 31, no. 12, pp. 8068–8073, Dec. 2016.

**J4.** **Z. Xin**, X. Wang, P. C. Loh, and F. Blaabjerg, "Grid-current-feedback control for LCL-filtered grid converters with enhanced stability," *IEEE Trans. Power Electron*., vol. 32, no. 4, pp. 3216–3228, Apr. 2017.

**J5.** **Z. Xin**, R. Zhao, P. Mattavelli, P. C. Loh, and F. Blaabjerg, "Re-investigation of generalized integrator based filters from a first-order-system perspective," *IEEE Access*, vol. 4, pp. 7131–7144, Nov. 2016.

**J6.** **Z. Xin**, P. Mattavelli, W. Yao, F. Blaabjerg, and P. C. Loh, "Mitigation of grid-current distortion for LCL-filtered voltage source inverter with inverter-current feedback control," *IEEE Trans. Power Electron*., under review.

Besides, there are two journal papers related to the extended application of the SOGI-QSG, which were published during the PhD period and are shown as follows. These two papers were not evaluated by the PhD Thesis Assessment Committee.

**J7.** **Z. Xin**, R. Zhao, F. Blaabjerg, L. Zhang, and P. C. Loh, "An improved flux observer for field-oriented control of induction motors based on dual second-order generalized integrator frequency-locked loop," *IEEE J. Emerg. Sel. Topics Power Electron.*, vol. 5, no. 1, pp. 513–525, Mar. 2017.

**J8.** R. Zhao, **Z. Xin**, P. C. Loh, and F. Blaabjerg, "A novel flux estimator based on multiple second-order generalized integrators and frequency-locked loop for induction motor drives," *IEEE Trans. Power Electron*., in press, 10.1109/TPEL.2016.2620428.

A list of conference papers related to this thesis is given as follows. Some of them have been submitted to journals for peer review. Only paper **C5** was evaluated by the PhD Thesis Assessment Committee.

### *Conference Papers*

**C1.** **Z. Xin**, X. Wang, P. C. Loh, and F. Blaabjerg, "SOGI-based capacitor voltage feedback active damping in LCL-filtered grid converters," in *Proc. of PEDG'15*, pp. 1–6, Jun. 2015.

**C2.** **Z. Xin**, X. Wang, P. C. Loh, and F. Blaabjerg, "Enhanced stability of capacitor-current feedback active damping for LCL-filtered grid converters," in *Proc. of ECCE'15*, pp. 4729–4736, Sep. 2015.

**C3.** **Z. Xin**, X. Wang, P. C. Loh, and F. Blaabjerg, "Digital realization of capacitor-voltage feedback active damping for LCL-filtered grid converters," in *Proc. of ECCE'15*, pp. 2690–2697, Sep. 2015.

**C4.** **Z. Xin**, R. Zhao, X. Wang, P. C. Loh, and F. Blaabjerg, "Four new applications of second-order generalized integrator quadrature signal generator," in *Proc. of APEC'16*, pp. 2207–2214, Mar. 2016.

**C5.** **Z. Xin**, C. Yoon, R. Zhao, P. C. Loh, and F. Blaabjerg, "Realization of quadrature signal generator using accurate magnitude integrator," in *Proc. of ECCE'16*, pp. 1–8, Sep. 2016.

**C6.** **Z. Xin**, Z. Qin, M. Lu, P. C. Loh, and F. Blaabjerg, "A new second-order generalized integrator based quadrature signal generator with enhanced performance," in *Proc. of ECCE'16*, pp. 1–7, Sep. 2016.

**C7. Z. Xin**, P. Mattavelli, W. Yao, F. Blaabjerg, and P. C. Loh, "Mitigation of grid-current distortion for LCL-filtered voltage-source inverter with inverter-side current control," in *Proc. of ECCE Asia'17*, accepted.

# CHAPTER 2. STABILITY ANALYSIS AND ACTIVE DAMPING OF GRID-CONNECTED VSI WITH LCL-FILTER

This chapter focuses on the practical implementation issue of the active damping control as shown in Figure 2-1. It begins with the modeling of the single-loop GCF and ICF control systems, based on which, their stable and unstable regions are identified. Next, the problems of the digital differentiator in the active damping loop are analyzed. To cope with these issues, two digital differentiators based on the non-ideal GI and the SOGI-QSG are proposed, whose effectiveness is finally validated by experimental results.

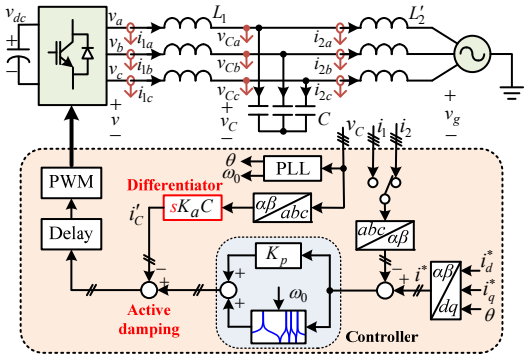


*Figure 2-1 Control system implementation of the LCL-filtered VSI with active damping.*

## 2.1. SYSTEM MODELING [J4, J6]

With the symbols defined in Figure 2-1, the VSI system, when the active damping loop is not considered, can be described by the following transfer functions:

$$v = F(s)e^{-sT_d}\left(i^* - i_{1(2)}\right), \tag{2.1}$$

$$sL_1 i_1 = v - v_C, \tag{2.2}$$

$$sL_2' i_2 = v_C - v_g, \tag{2.3}$$

$$sCv_C = i_1 - i_2, \tag{2.4}$$

where the filter parasitic resistances are neglected. The grid-side inductor $L_2$ and the grid impedance $L_g$ are combined as $L'_2$ for simplicity. $F(s)$ is the transfer function of the current controller. $T_d$ is the total time delay in the system, which is approximated as $1.5T_s$ considering sampling, computation, updating of the compare registers, and the zero-order-hold effect of PWM [36]. The scalar notation is used for simplicity, which should be modified as space vectors for the $\alpha\beta$-frame implementation. The transfer functions for relating the inverter output voltage $v$ to the output current $i_1$, grid current $i_2$, and capacitor current $i_C$ are given by:

$$G_{i1}(s) = \frac{i_1(s)}{v(s)} = \frac{1}{sL_1}\frac{s^2+\omega_0^2}{s^2+\omega_r^2} \tag{2.5}$$

$$G_{i2}(s) = \frac{i_2(s)}{v(s)} = \frac{1}{sL_1}\frac{\omega_0^2}{s^2+\omega_r^2} \tag{2.6}$$

$$G_{ic}(s) = \frac{i_C(s)}{v(s)} = \frac{1}{sL_1}\frac{s^2}{s^2+\omega_r^2} \tag{2.7}$$

where $\omega_0$ and $\omega_r$ are the anti-resonance frequency and resonance frequency of the LCL-filter, whose expressions are given by:

$$\omega_r = \sqrt{\frac{L_1+L_2'}{L_1L_2'C}}, \quad f_r = \frac{\omega_r}{2\pi}, \tag{2.8}$$

$$\omega_0 = \sqrt{\frac{1}{L_2'C}}, \quad f_0 = \frac{\omega_0}{2\pi}. \tag{2.9}$$

For each control strategy (ICF and GCF), a PR controller plus HCs can be used for current regulation. Transfer function of the controller is given by (2.10), where $K_p$, $h$, $K_{rh}$, $J$ and $\omega_0$ represent the proportional gain, harmonic order to be suppressed, resonant gain of each harmonic component, maximum harmonic order specified for attenuation, and the fundamental grid frequency, respectively.

$$F(s) = K_p + \sum_{h=1}^{J}\frac{K_{rh}s}{s^2+(h\omega_0)^2}. \tag{2.10}$$

With the above transfer functions, the control block diagrams of the ICF and GCF control systems are shown in Figure 2-2. The transfer functions $i_C(s)/i_1(s)$ and $i_2(s)/i_C(s)$ can be derived by dividing (2.5) from (2.7) and (2.7) from (2.6) respectively, which are given as:

$$\frac{i_C(s)}{i_1(s)} = \frac{G_{iC}(s)}{G_{i1}(s)} = \frac{s^2}{s^2+\omega_0^2}, \tag{2.11}$$

$$\frac{i_2(s)}{i_C(s)} = \frac{G_{i2}(s)}{G_{iC}(s)} = \frac{\omega_0^2}{s^2}. \tag{2.12}$$

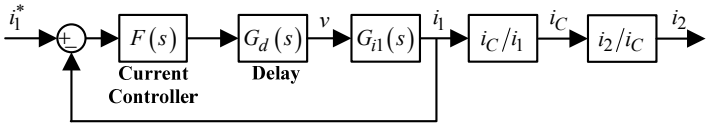


(a)

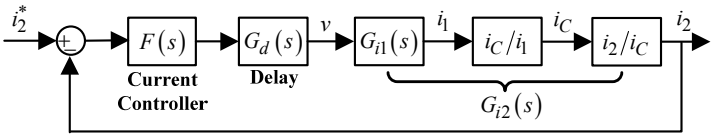


(b)

*Figure 2-2 Control block diagrams of the single-loop (a) Inverter Current Feedback (ICF) scheme and (b) Grid Current Feedback (GCF) scheme [37].*

The open-loop transfer functions of the single-loop ICF and GCF systems are:

$$T_{i1}(s) = F(s)e^{-sT_d}G_{i1}(s) \tag{2.13}$$

$$T_{i2}(s) = F(s)e^{-sT_d}G_{i2}(s) \tag{2.14}$$

## 2.2. STABILITY ANALYSIS AND ACTIVE DAMPING [J4]

The Nyquist Stability Criterion (NSC) is applied to investigate the stability of the system. In the open-loop Bode plot, the phase crossings at the $\pm(2k+1)\times180°$ ($k$ is an integer) lines from below to top and from top to below are defined as the positive crossing and negative crossing respectively. For convenience, the number of positive crossings is noted as $N^+$ and the number of negative crossings is notated as $N^-$. The NSC states that the open-loop poles must be equal to $2(N^+ - N^-)$ in order to ensure the system stability.

### 2.2.1. STABILITY OF THE SINGLE-LOOP INVERTER-CURRENT FEEDBACK (ICF) AND GRID-CURRENT FEEDBACK (GCF) CONTROL SYSTEMS

It can be found that the number of the open-loop unstable poles is zero for both $T_{i1}$ and $T_{i2}$. To ensure the system stability, the number of positive crossings and the number of negative crossings should be the same (i.e. $N^+ = N^-$) according to the NSC. To illustrate it, the open-loop Bode plots of the two single-loop schemes are

plotted in Figure 2-3 with four different LCL-filter resonance frequencies obtained by changing the value of the filter capacitor according to Table 2-1.

*Table 2-1 LCL Parameters and Resonance Frequencies [37]*

| Converter-side inductance $L_1$ | 3 mH | Grid-side inductance $L_2 + L_g$ | | 1.8 mH |
|---|---|---|---|---|
| Capacitance $C$ | 25 µF | 11 µF | 5 µF | 2 µF |
| Resonance Frequency | $f_{r1}$ = 0.95 kHz | $f_{r2}$ = 1.43 kHz | $f_{r3}$ = 2.12 kHz | $f_{r4}$ = 3.36 kHz |

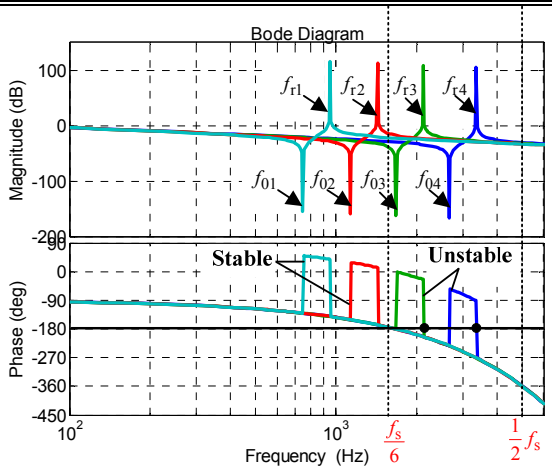


(a)

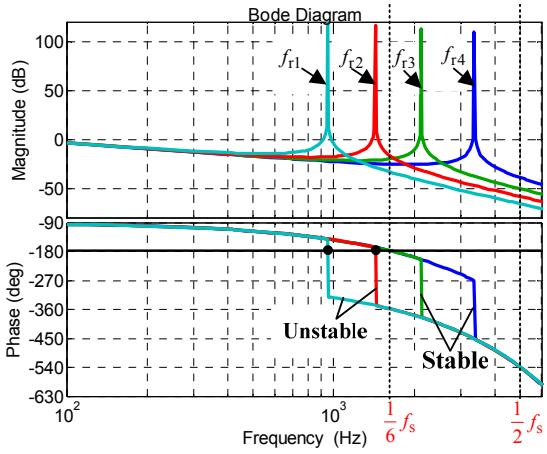


(b)

*Figure 2-3 Open-loop Bode plots of the single-loop (a) ICF and (b) GCF schemes with four LCL resonance frequencies [37].*

For the ICF scheme, two phase jumps accompanied by a magnitude trough and a magnitude peak can be observed in each open-loop Bode plot as shown in Figure 2-3(a). The resonance and anti-resonance frequencies can be derived from (2.8) and (2.9) respectively [38]. When $f_r$ is larger than $f_s/6$ (e.g. $f_{r3}, f_{r4}$), an effective negative crossing will be generated at $f_r$ (e.g. $f_{r3}$, $f_{r4}$) accompanied by a positive magnitude peak. On the contrary, the phase crossing $-180°$ at $f_{03}$ or $f_{04}$ is not a positive crossing, since the magnitude is always smaller than 0 dB. Consequently, the numbers of positive crossings and negative crossings are different and the system is unstable according to the NSC. On the other hand, if $f_r$ is smaller than $f_s/6$ (e.g. $f_{r1}$, and $f_{r2}$), the numbers of positive crossings and negative crossings will both be zero. In this case, the system can be stable as long as the proportional gain of the current controller is designed properly. In conclusion, the stable region of the single-loop ICF scheme is $(0, f_s/6)$ and the unstable region is $(f_s/6, f_s/2)$.

The stability characteristic becomes opposite for the single-loop GCF scheme, whose open-loop Bode plot is shown in Figure 2-3(b). It is noted that only one phase jump occurs at $f_r$, where a positive magnitude peak always exists. Despite this phase jump, neither negative crossing nor positive crossing occurs when $f_r$ is larger than $f_s/6$ (e.g. $f_{r3}, f_{r4}$). The system can thus be stable when $f_r$ is located in $(f_s/6, f_s/2)$ with a properly designed proportional gain of the current controller. On the other hand, an effective negative crossing occurs when $f_r$ is smaller than $f_s/6$ (e.g. $f_{r1}, f_{r2}$), since the magnitude is always larger than 0 dB due to the magnitude peak. Therefore, the system is unstable in $(0, f_s/6)$, because no corresponding positive crossing is present. As a result, the unstable region of the single-loop GCF scheme is $(0, f_s/6)$ and the stable region is $(f_s/6, f_s/2)$.

Since the frequency $f_s/6$ separates the stable and unstable regions of the two systems, it is thus called the critical frequency [39], whose value is mainly determined by the phase lag of the time delay in the digital control system [36].

### 2.2.2. ACTIVE DAMPING AND PRACTICAL IMPLEMENTATION ISSUES

To damp the LCL-resonance, active damping schemes that need no passive element have been suggested in practice [15]–[19]. Generally, active damping can be realized by either inserting a notch filter into the forward loop of the control system or feeding back some variables in the control loop. The basic principle of the notch-filter based active damping can be illustrated by the Bode plot in Figure 2-4, where a GCF control system is taken as an example. The notch-filter based active damping uses the magnitude through of a notch filter to cancel out the magnitude peak introduced by the LCL-filter. At the same time, the phase jump associated with the magnitude peak can be compensated by the notch filter, which reduces the risk of system instability. However, the notch frequency of the filter should be accurately tuned at the LCL-filter resonance frequency in order to guarantee the effectiveness, which is difficult to realize in practice due to the uncertainty of the resonance

frequency caused by grid impedance variation. To solve the problem, a self-commissioning notch filter is proposed in [40], where the resonance frequency is detected online to tune the notch frequency. Despite its effectiveness, this method suffers from complexity and also high computational burden.

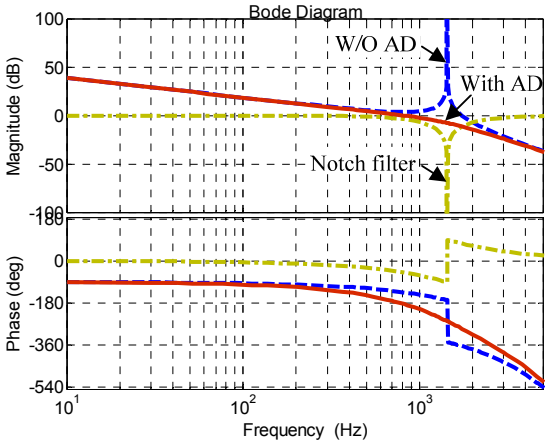


*Figure 2-4 Bode plots of the GCF scheme with and without the notch-filter based active damping.*

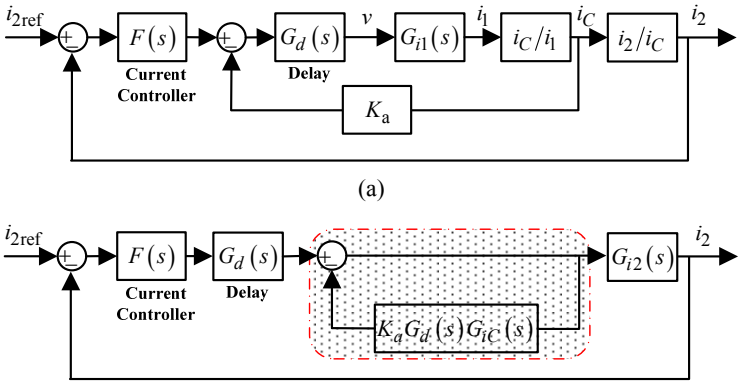


*Figure 2-5 Control block diagrams of the GCF control system with the capacitor-current feedback active damping (a) basic structure (b) equivalent structure [37].*

To realize a real-time tracking of the resonance frequency, the notch filter can be realized by feeding back some variables in the control loop. The effective variables can be the capacitor current [18], [20], [21], the capacitor voltage [17], [19], [22], and the grid current [23], [24]. The control diagram of the capacitor-current feedback active damping is shown in Figure 2-5(a) and the equivalent structure is

shown in Figure 2-5(b). Through an equivalent transformation, the active damping function can be described by the transfer function of the shaded part in Figure 2-5(b), whose Bode plot is given in Figure 2-6(a) accompanied by the open-loop Bode plots of the single-loop and the dual-loop GCF schemes. To illustrate it, the time delay in the shaded part is first ignored. It is interesting to note that Figure 2-6(a) is almost the same with Figure 2-4, where the magnitude trough and the phase jump provided by the inner loop cancel out the magnitude-peak and phase jump introduced by the LCL-filter. Hence, the working principle of the capacitor-current feedback active damping is in agreement with the notch-filter based active damping, while the former is superior to the latter since its notch frequency is self-adaptive.

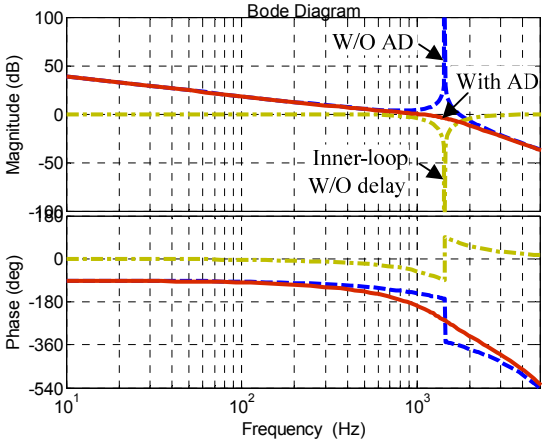


(a)

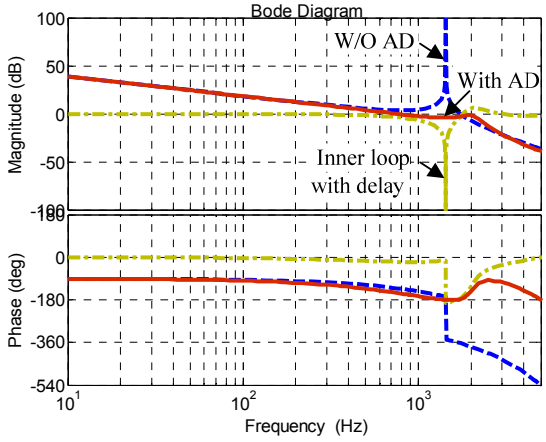


(b)

*Figure 2-6 Open-loop Bode plot of the GCF scheme with the capacitor-current feedback active damping (a) with the inner-loop delay (b) without the inner-loop delay.*

Unfortunately, in practice, the time delay in the inner loop influences the damping performance, which can be seen from the Bode plot in Figure 2-6(b) when the inner-loop time delay is considered. Detailed discussion about this issue and a solution will be provided in Chapter 3.

Another challenge of the capacitor-current feedback active damping is the increased numbers of sensors for capacitor current measurement. In practice, the capacitor voltage is measured for grid synchronization, which can thus be used to calculate the capacitor current at the same time in order to reduce the total cost of sensors. This approach is especially attractive for applications at MW range below 1000V, where the cost of a current sensor is much higher than that of a voltage sensor. Capacitor-voltage feedback active damping has thus been applied in [22], where it is found that among proportional, integral and derivative feedbacks, only the derivative of the capacitor voltage has damping effect. However, accurate implementation of a digital differentiator is difficult. For instance, the differentiator discretized by the Tustin method can preserve the 90° phase lead, but the magnitude becomes infinite at the Nyquist frequency as observed from Figure 2-7, which may introduce noise amplification. In terms of the backward Euler discretization, it faces the problem of large phase error at high frequency where the LCL-filter resonance frequency may locate and the active damping may lose its effectiveness. The forward Euler method has a phase lead characteristic which realizes delay compensation at the same time. However, unstable poles of the closed system are produced when the forward Euler discretization is used to differentiate the capacitor voltage.

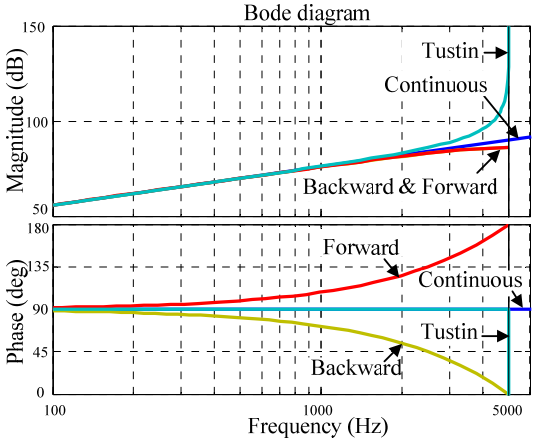


*Figure 2-7 Frequency response of the differentiators discretized by the traditional discretization methods [41].*

Alternatively, the lead-lag differentiator was proposed in [17] and [19] for resonance damping, which works as a differentiator around the resonance frequency. However, similar to the problem of the notch-filter based active damping, it is very sensitive to

grid impedance variation, which makes it only suitable for a strong grid. To improve the performance of the digital differentiator, two new differentiators are presented hereinafter based on either the non-ideal GI or the SOGI-QSG.

## 2.3. NON-IDEAL GENERALIZED INTEGRATOR (GI) BASED ACTIVE DAMPING [J2]

### 2.3.1. BASIC PRINCIPLE

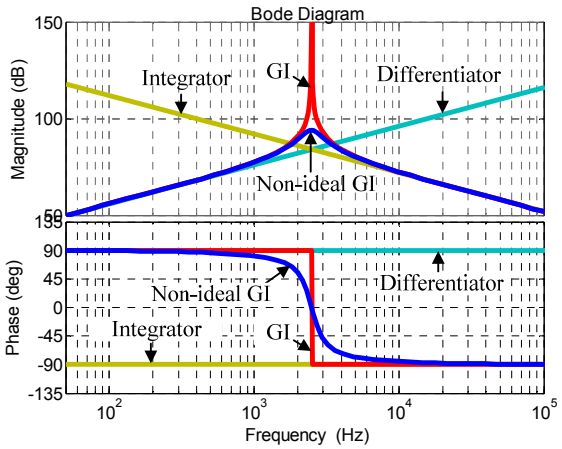


*Figure 2-8 Bode plots of the ideal Generalized Integrator (GI), the non-ideal GI, the ideal differentiator and the pure integrator [41].*

The GI has widely been used as controllers, whose transfer function is written as:

$$GI(s) = \frac{\omega'^2 s}{s^2 + \omega'^2} \tag{2.15}$$

where $\omega'$ is the center frequency of GI at which it has an infinite gain, and $\omega'^2$ is added here for better illustrating the differentiation characteristic of GI. Substituting $s = j\omega$ to (2.15), the magnitude and phase expressions can be given by:

$$\left|GI(j\omega)\right| = \frac{\omega'^2 \omega}{\left|\omega'^2 - \omega^2\right|}, \tag{2.16}$$

$$\angle GI(j\omega) = \mathrm{sgn}\left(\omega'^2 - \omega^2\right) \cdot 90° . \tag{2.17}$$

When $\omega \ll \omega'$, (2.16) and (2.17) can be simplified to $\omega$ and 90°, which is equivalent to an ideal differentiator. Oppositely, when $\omega \gg \omega'$, the GI is equivalent to a pure integrator. These characteristics can be observed clearly from Figure 2-8 which

shows the Bode plot of (2.15). However, it is noted that the GI also has an infinite gain, which is susceptible to noise amplification. To avoid the problem, the non-ideal GI can be used, whose transfer function is given by

$$GI'(s) = \frac{\omega'^2 s}{s^2 + \omega_c s + \omega'^2} \tag{2.18}$$

where $\omega_c$ determines the damping extent of the non-ideal GI whose Bode plot is shown in Figure 2-8. To flatten the infinite peak of GI, $\omega_c$ should be designed higher than that for a resonant controller, which is 5000 rad/s in Figure 2-8. The other difference from the typical application is the design of $\omega'$, which is set to the Nyquist frequency in order to obtain the widest differentiation characteristic.

### 2.3.2. DISCRETIZATION OF THE NON-IDEAL GI

The non-ideal GI differentiator should be discretized appropriately before it is used in a digital system. The discretization methods can be Tustin, pre-warped Tustin, backward Euler, forward Euler, Zero-Pole Matching (ZPM), First-Order Hold (FOH), Zero-Order Hold (ZOH), or Impulse Invariant (IMP) method [42]. The corresponding Bode plots are shown in Figure 2-9(a) and (b). It can be observed that, the forward and backward Euler methods produce the best magnitude match, but unstable poles or large phase errors are produced. The Tustin method shifts the frequency of the magnitude peak, which can be avoided by the pre-warped Tustin. But the pre-warped magnitude response has a high gain at the Nyquist frequency, which may introduce noise amplification. Figure 2-9(b) further shows that the ZOH, ZPM and IMP methods are not suitable due to the large phase mismatches. Finally, the FOH method, which provides the closest characteristic to the *s*-domain non-ideal GI differentiator, is selected for digital implementation.

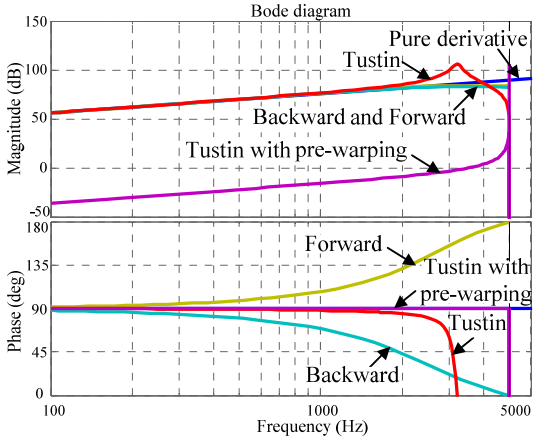


(a)

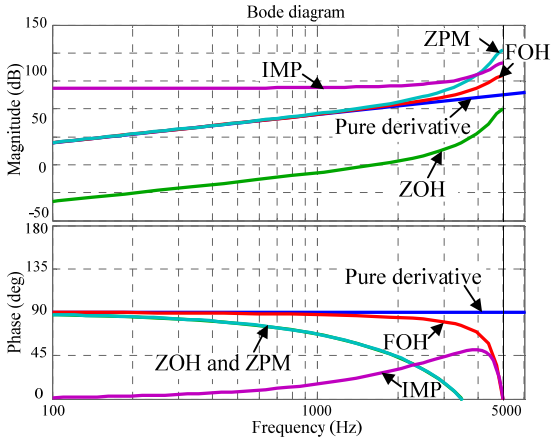


(b)

*Figure 2-9 Frequency responses of 8 different discretized non-ideal GI differentiators [41].*

### 2.3.3. COMPARISON WITH EXISTING DIFFERENTIATORS

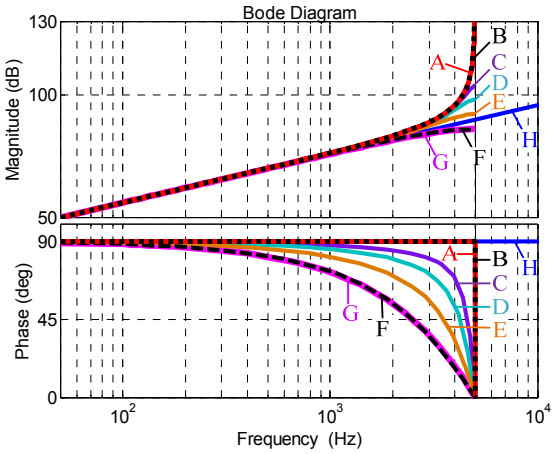


*Figure 2-10 Frequency responses of differentiators (A) discretized with Tustin method, (G) discretized with backward Euler method, and (B to F) FOH-discretized non-ideal GI with $\omega_c$ = 0, 5000, 10000, 20000 and 42000 rad/s [41].*

Performance of the proposed non-ideal GI differentiator is compared with that of the Tustin and backward Euler differentiators. *Figure 2-10* shows the Bode plots of these methods, where for the non-ideal GI four values are chosen for $\omega_c$ which are 0, 5000, 10000, 20000 and 42000 rad/s. It is noted that the ideal GI and the Tustin differentiators have the same frequency response, which can be illustrated by the FOH-discretized GI function in (2.19).

$$GI(z)_{FOH} = \frac{1-\cos(\omega' T_s)}{T_s} \frac{z-1}{z^2 - 2z\cos(\omega' T_s) + 1} \tag{2.19}$$

Since $\omega'$ has been set to the Nyquist frequency, (2.19) can be simplified to (2.20) which is the same with the function of Tustin discretization.

$$GI(z)_{FOH} = \frac{2}{T_s} \frac{z-1}{z+1} \tag{2.20}$$

Interestingly, when $\omega_c$ increases to 42000 rad/s, the characteristic of the non-ideal GI differentiator is close to that of the backward Euler differentiator. Considering $\omega_c$ can be tuned easily, the characteristic of the non-ideal GI differentiator can be designed conveniently according to the requirements of the phase error and noise attenuation performance.

### 2.3.4. EXPERIMENTAL VALIDATION

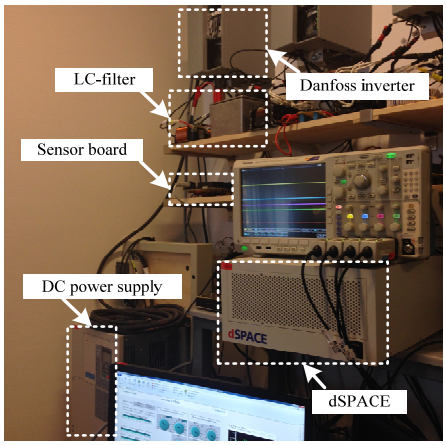


*Figure 2-11 Experimental setup [41].*

To validate the effectiveness of the non-ideal GI differentiator, an LCL-filtered grid-connected VSI system was built in the laboratory as shown in Figure 2-11. A detailed description about the experimental setup can be found in **J2**. In the control system, the grid current was measured for control and the capacitor voltage is measured for grid synchronization and active damping. A differentiator was inserted into the inner damping loop for computing the capacitor current from the capacitor voltage. It can be observed from Figure 2-12 that the system is stable with the non-ideal GI differentiator but unstable with the backward Euler differentiator. The reason is the large phase error of the backward Euler differentiator, which makes the active damper poor in effectiveness.

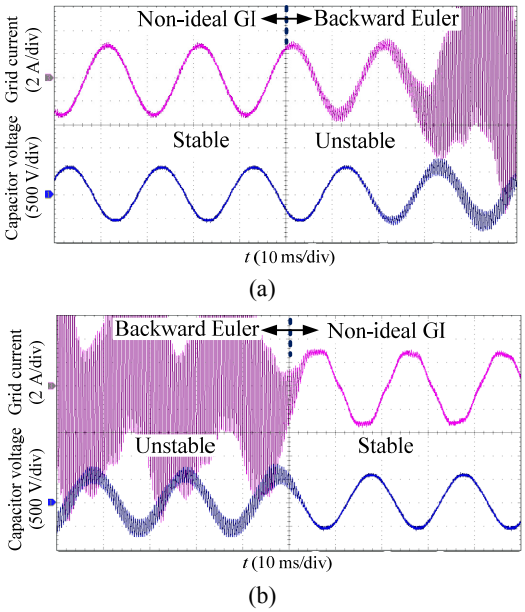


*Figure 2-12 Experimental waveforms when the differentiator changes between non-ideal GI and backward Euler [41].*

## 2.4. SECOND-ORDER GI (SOGI) BASED ACTIVE DAMPING [J2]

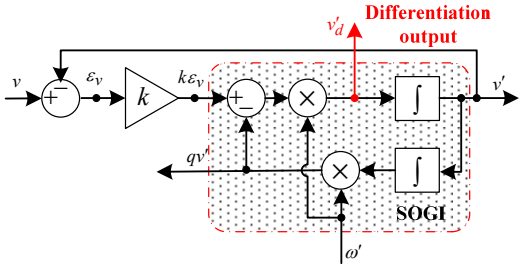


*Figure 2-13 Principle of SOGI based differentiator [41].*

The structure of the SOGI-QSG is shown in Figure 2-13, where the output $v'$ and $qv'$ are the in-phase and quadrature signals of the input, which has been widely used for power converter applications such as single-phase grid synchronization. Apart from these two outputs, there is another output which is the differentiation of the input and can be used to implement the active damping function. To begin with, the transfer function for relating $v'$ to the input $v$ can be expressed as

$$D(s)=\frac{v'}{v}=\frac{k\omega' s}{s^2+k\omega' s+\omega'^2}. \tag{2.21}$$

where $\omega'$ is the center frequency and $k$ is the damping factor. At the frequency $\omega'$, the output $v'$ is in-phase with the input $v$, and the output $v_d'$ is the differentiation of the input at $\omega'$. If the input of SOGI-QSG is the capacitor voltage, the output $v_d'$ will be the capacitor current when $\omega'$ is tuned at the LCL-filter resonance frequency. To illustrate it, the transfer function for relating the output $v_d'$ to the input $v$ is first given by (2.22), which, for digital implementation, should be discretized by the pre-warped Tustin method.

$$G_{v_d'}(s) = \frac{v}{v'} = \frac{k\omega' s^2}{s^2 + k\omega' s + \omega'^2}. \tag{2.22}$$

Next, Bode plots of (2.22) and its discretized transfer function are shown in Figure 2-14. It can be found that the working principle of the SOGI-based differentiator is similar to the lead-lag differentiator, while the former has a more accurate phase characteristic. Moreover, the SOGI-based differentiator has a smaller gain than the ideal differentiator both above and below the working frequency, which is helpful for noise attenuation. However, active damping based on SOGI-based differentiator needs online grid-impedance estimation or resonance-frequency detection to tune its working frequency. These algorithms make the overall scheme more complicated [28].

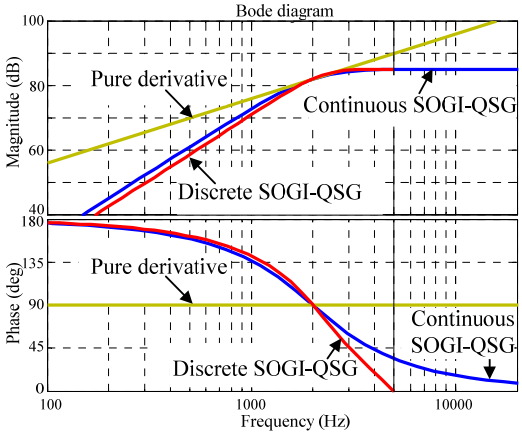


*Figure 2-14 Frequency responses of the discretized SOGI-QSG, the continuous SOGI-QSG and the ideal "s" derivatives [41].*

It is known that the time delay in the control loop weakens the stability of the single-loop GCF control system, which can be improved through time delay compensation. It is noted from Figure 2-14 that the SOGI-based differentiator has a phase-lead characteristic below the 90°-crossing frequency and a phase-lag characteristic above the 90°-crossing frequency. The phase-lead characteristic contributes to time-delay compensation and enhances the stability of the control system. For the parameter

design of the SOGI-based differentiator, it is therefore advised to set its 90°-crossing frequency at the resonance frequency where the grid inductance is zero. In this case, even if the grid inductance varies, the resonance frequency can only become smaller than the 90°-crossing frequency of the SOGI-based differentiator, and its phase-lead characteristic will enhance the system stability. In this case, an additional grid impedance estimation algorithm can be avoided. Detailed description about the principle and parameter design can be found in **J2**.

## 2.5. SUMMARY

In this chapter, the digital implementation issues of the active damping control are analyzed. To overcome the problems, two digital differentiators based on non-ideal GI and SOGI-QSG are proposed. Performance of the non-ideal GI differentiator can be adjusted conveniently according to the application requirement, which alleviates the noise-amplification and phase-error issues of the traditional Tustin differentiator and backward Euler differentiator. On the other hand, the SOGI-based differentiator has a fixed characteristic, but it can achieve delay compensation at the same time. The proposed two differentiators can also be employed in other applications, even though they have only been discussed for active damping in this thesis.

# CHAPTER 3. STABILITY ENHANCEMENT OF THE CURRENT CONTROL SYSTEMS USING TIME-DELAY COMPENSATION [J4]

This chapter focuses on the stability enhancement of the current control system using time-delay compensation approach as shown in Figure 3-1. To begin with, an optimized inner-loop damping gain is determined for the dual-loop GCF scheme with active damping, which is able to fix the stable region of the system always below the critical frequency, regardless of the variation of the grid impedance and LCL-filter parameters. Finally, an improved time-delay compensation method is presented to enhance the system stability.

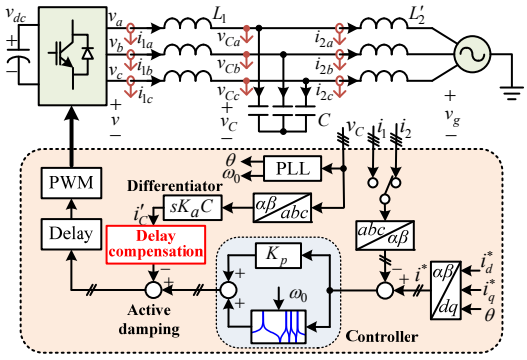


*Figure 3-1 Control system implementation of the LCL-filtered VSI with active damping.*

## 3.1. STABILITY ENHANCEMENT TECHNIQUES FOR SINGLE-LOOP ICF AND GCF SCHEMES

As mentioned previously, the critical frequency is the division between the stable and the unstable regions of the two control systems. To enhance the stability of the single-loop ICF scheme, the stable region can be widened by increasing the critical frequency with time delay compensation methods such as shifting the sampling constants [18], inserting a prediction block into the control loop [43], or using the state observers [44]. On the other hand, to widen the stable region of the single-loop GCF scheme, the critical frequency should be decreased, which means that the time delay should be enhanced rather than reduced. However, a large time delay reduces the controller bandwidth and degrades the control performance significantly [43].

Therefore, the stable region of the GCF scheme cannot be widened directly by decreasing the critical frequency.

To cope with this issue, the capacitor-current feedback AD control method shown in Figure 2-5(a) is advised for the GCF control system. If the stability characteristic of the dual-loop GCF control can be the same with that of the single-loop ICF control, i.e. stable in $(0, f_s/6)$ and unstable in $(f_s/6, f_s/2)$, the stable region can then be widened using time-delay compensation techniques like the single-loop ICF control.

Unfortunately, it is not always true that the expected stable region $(0, f_s/6)$ can be retained with the active damping control. For example, if the grid impedance varies in a wide range, or the damping gain $K_a$ and the controller gain $K_p$ are not designed properly, the expected stable region $(0, f_c)$ may become the unstable region again. To clearly illustrate this problem, Figure 3-2(a) and (b) show the root loci of the dual-loop GCF control system with four resonance frequencies and two AD gains for each resonant frequency. Before plotting the root locus, the *s*-domain open-loop transfer function of the dual-loop GCF scheme should be discretized first. To do this, the control diagram in Figure 2-5(a) is equivalently transformed to that in Figure 3-3, where the damping gain $K_a$ is written as $mK_p$ in order to study the influence of the relation between $K_a$ and $K_p$ on the system stability.

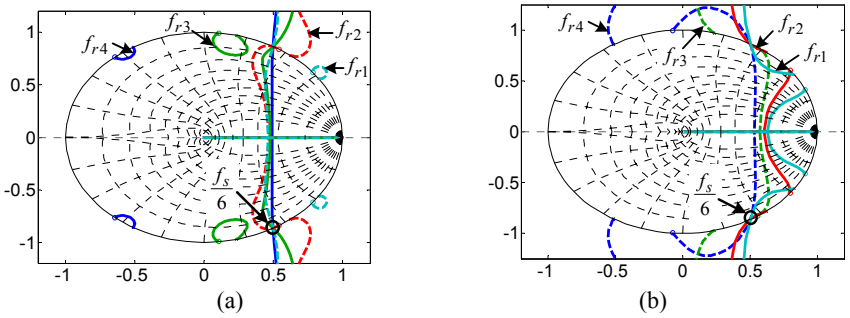


*Figure 3-2 Root loci of the dual-loop GCF control system with two damping gains (a) $K_a$ = 0.5 $K_p$, (b) $K_a$ = 1.25 $K_p$ [37].*

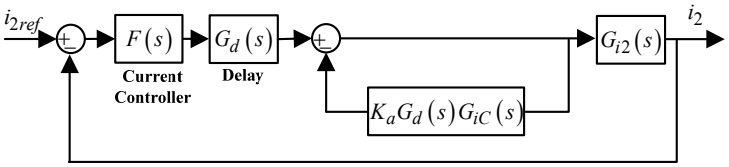


*Figure 3-3 Equivalent block diagram of the dual-loop GCF control scheme [37].*

From Figure 3-3, the *s*-domain open-loop transfer function of the dual-loop GCF control system is given by:

$$T_{ad}(s) = F(s)G_d(s)G_{inner}(s)G_{i2}(s) \tag{3.1}$$

where $G_{inner}(s)$ is the inner closed-loop transfer function, which can be expressed by:

$$G_{inner}(s) = \frac{1}{1 + mK_pG_d(s)G_{iC}(s)}. \tag{3.2}$$

For digital implementation, the transfer functions $G_{i2}(s)$ and $G_{iC}(s)$ are discretized by the ZOH discretization as follows:

$$G_{i2}(z) = \frac{\omega_r T_s\left[z^2 - 2z\cos(\omega_r T_s) + 1\right] - \sin(\omega_r T_s)(z-1)^2}{\omega_r(L_1 + L_2')(z-1)\left[z^2 - 2z\cos(\omega_r T_s) + 1\right]}, \tag{3.3}$$

$$G_{iC}(z) = \frac{\sin(\omega_r T_s)}{\omega_r L_1}\frac{z-1}{z^2 - 2z\cos(\omega_r T_s) + 1}. \tag{3.4}$$

For simplicity, it is assumed that the resonant gains of the PR controller are properly designed, and thus the phase lag caused by them can be negligible. In this case, the $z$-domain transfer function of the PR controller $F(z)$ can be expressed by a simple proportional gain $K_p$. The corresponding $z$-domain transfer function of (3.2) is given by:

$$\begin{aligned} G_{inner}(z) &= \frac{1}{1 + mK_pz^{-1}G_{iC}(z)} \\ &= \frac{1}{1 + mK_pz^{-1}\dfrac{\sin(\omega_r T_s)}{\omega_r L_1}\dfrac{z-1}{z^2 - 2z\cos(\omega_r T_s) + 1}} \end{aligned} \tag{3.5}$$

The $z$-domain open-loop transfer function of the dual-loop GCF can thus be expressed by:

$$\begin{aligned} T_{ad}(z) &= K_pz^{-1}G_{inner}(z)G_{i2}(z) \\ &= K_pz^{-1}\frac{1}{1 + mK_pz^{-1}\dfrac{\sin(\omega_r T_s)}{\omega_r L_1}\dfrac{z-1}{z^2 - 2z\cos(\omega_r T_s) + 1}} \cdot \\ &\quad \frac{\omega_r T_s\left[z^2 - 2z\cos(\omega_r T_s) + 1\right] - \sin(\omega_r T_s)(z-1)^2}{\omega_r(L_1 + L_2')(z-1)\left[z^2 - 2z\cos(\omega_r T_s) + 1\right]} \end{aligned} \tag{3.6}$$

The root locus of the dual-loop GCF system is determined by the denominator poles of the closed-loop transfer function with the change of the controller gain. The

relevant expression can be derived using the formulation of $1 + T_{ad}(z) = 0$, which can be given by (3.7):

$$1+K_p\frac{m\sin(\omega_r T_s)(L_1+L_2')(z-1)^2+\omega_r L_1 T_s\left[z^2-2z\cos(\omega_r T_s)+1\right]-L_1\sin(\omega_r T_s)(z-1)^2}{\omega_r L_1(L_1+L_2')z(z-1)\left[z^2-2z\cos(\omega_r T_s)+1\right]}=0 \quad (3.7)$$

With the above expressions, the root loci are finally plotted in Figure 3-2. It can be seen from Figure 3-2(a) that the frequencies $f_{r3}$ and $f_{r4}$, which are higher than $f_s/6$, are in the stable region, while the frequencies $f_{r1}$ and $f_{r2}$, which are lower than $f_s/6$, are in the unstable region. In contrary, Figure 3-2(b) shows that the higher frequencies ($f_{r3}$ and $f_{r4}$) are in the unstable region, and the lower frequencies ($f_{r1}$ and $f_{r2}$) are in the stable region. It can be seen that different damping gains result in different stability characteristics for the dual-loop GCF scheme. As mentioned previously, in order to widen the stable region of the GCF control system without increasing the time delay, the stable region of the system should be fixed at the low frequency region $(0, f_s/6)$. However, this is not easy to realize with the existing design method for the damping gain, but it can be easily realized with the proposed design rule in this chapter.

## 3.2. NECESSARY ACTIVE DAMPING GAIN TUNING REQUIREMENT

The single-loop ICF scheme can be equivalently transformed to a dual-loop GCF scheme as shown in Figure 3-4, whose inner damping gain is fixed to $K_p$. Hence, the dual-loop GCF system has the same stability characteristic with the single-loop ICF control, i.e. stable in $(0, f_s/6)$ and unstable in $(f_s/6, f_s/2)$.

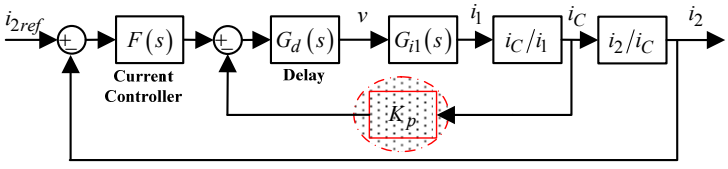


*Figure 3-4 Equivalent transformation of the single-loop ICF to dual-loop GCF scheme [37].*

To prove it, the root loci of the three systems are presented in Figure 3-5 to illustrate the stability characteristic of the dual-loop GCF system when $K_a = K_p$ is selected. It is noted that the stable regions of the single-loop ICF in Figure 3-5(a) and the single-loop GCF in Figure 3-5(b) are in agreement with the results in Figure 2-3. As for the dual-loop GCF scheme with the damping gain $K_p$, its root loci are shown in Figure 3-5(c). It is interesting to find that Figure 3-5(c) is the same with Figure 3-5(a), which indicates that these two systems may have the same stability characteristic. The conclusion can be proved by deriving the closed-loop characteristic equation of the single-loop ICF system using the formulation of $1 + T_{i1}(z) = 0$, where $T_{i1}(z)$ expressed by (3.8) is the open-loop transfer function. The closed-loop characteristic

equation is given by (3.9). It is noted that (3.9) and (3.7) have the same characteristic roots, which thus lead to the same root loci in Figure 3-5(a) and (c).

$$T_{i1}(z) = K_p z^{-1} G_{i1}(z) = K_p \frac{L_1 \omega_r T_s \left[ z^2 - 2z\cos(\omega_r T_s) + 1 \right] + L_2' \sin(\omega_r T_s)(z-1)^2}{\omega_r L_1 (L_1 + L_2') z (z-1) \left[ z^2 - 2z\cos(\omega_r T_s) + 1 \right]} \quad (3.8)$$

$$1 + K_p \frac{L_1 \omega_r T_s \left[ z^2 - 2z\cos(\omega_r T_s) + 1 \right] + L_2' \sin(\omega_r T_s)(z-1)^2}{\omega_r L_1 (L_1 + L_2') z (z-1) \left[ z^2 - 2z\cos(\omega_r T_s) + 1 \right]} = 0 \quad (3.9)$$

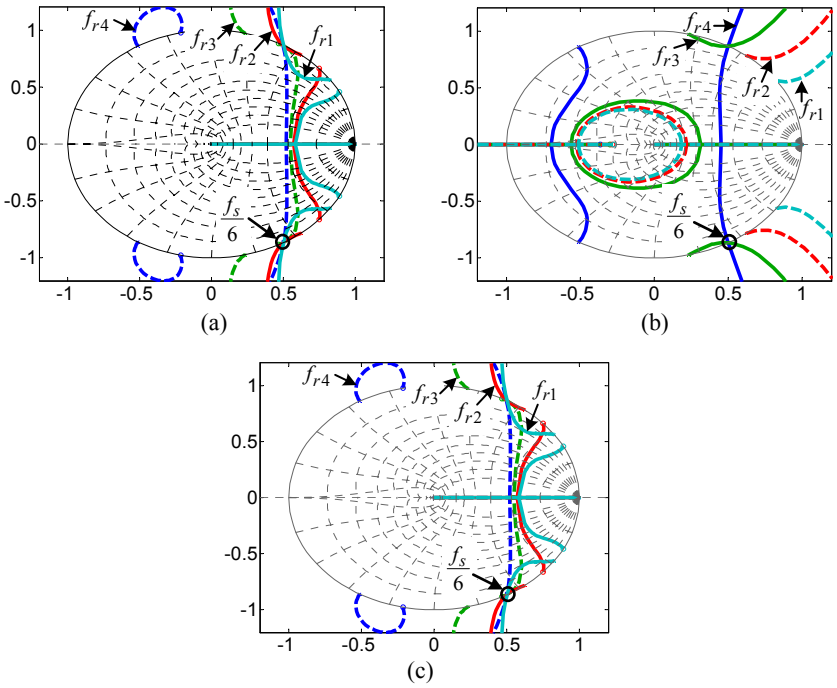


*Figure 3-5 Root loci of the single-loop ICF, single-loop GCF, and the dual-loop GCF with its damping gain set to $K_p$ [37].*

## 3.3. SOGI BASED TIME DELAY COMPENSATION

After finding out the damping gain to fix the stable region at $(0, f_s/6)$, next task is to research how to widen the stable region of the dual-loop GCF scheme. Although several time delay compensation techniques [18], [20], [21] have been proposed recently to enhance the system stability, they still suffer from some practical issues. To cope with them, a new time delay compensation method based on SOGI-QSG is presented as follows. In terms of the SOGI-QSG in Figure 2-13, the error signal $\varepsilon_v$ has a notch characteristic, whose corresponding transfer function is given by

$$E(s)=\frac{\varepsilon_v}{v}=1-D(s)=\frac{s^2+\omega'^2}{s^2+k\omega' s+\omega'^2}. \tag{3.10}$$

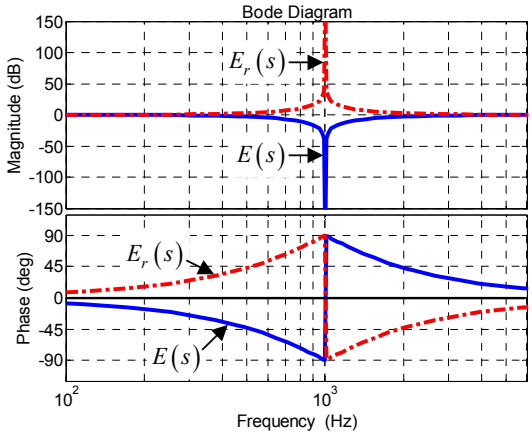


(a)

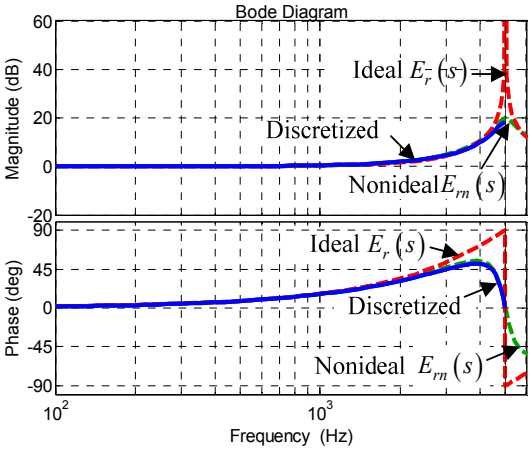


(b)

*Figure 3-6 Bode plots of (a) E(s) and $E_r(s)$, (b) $E_{rn}(s)$ and $E_r(z)$ when ω′ is tuned to the Nyquist frequency [37].*

The solid line in Figure 3-6 shows the Bode plot of (3.10) when $\omega'$ is set to 2π*1000 rad/s. Due to the notch-filter characteristic, the phase of $E(s)$ first reduces from 0 to -90° below $\omega'$, and then jumps from -90° to 90° at $\omega'$, and finally reduces back to 0. Below $\omega'$, the phase characteristic of $E(s)$ has a similar phase-lag characteristic of the time delay. Therefore, a very simple idea to compensate the phase lag of the time delay is using the opposite phase characteristic of $E(s)$, which can be obtained by calculating its reciprocal function as given by (3.11).

$$E_r(s) = \frac{1}{E(s)} = 1 + \frac{k\omega' s}{s^2 + \omega'^2} \tag{3.11}$$

The phase-lead characteristic of $E_r(s)$ can be clearly observed from the dashed Bode plot in Figure 3-6(a). To make full use of the phase-lead characteristic, $\omega'$ is set to the Nyquist frequency. However, an infinite gain exists at $\omega'$ as shown in Figure 3-6(b), which may introduce noise amplification. The infinite gain also exists in the method proposed in [20]. Differently, the infinite gain of the SOGI-based method can easily be avoided by replacing the resonant term in (3.11) with its non-ideal version. The resulting transfer function is given by (3.12). The FOH discretization was used to discretize (3.11) for digital implementation. The Bode plot of the discretized transfer function is shown in Figure 3-6(b) where the characteristics of $E_{rn}(s)$ and $E_{rn}(z)$ are very close to each other, implying that the FOH discretization is indeed a suitable technique.

$$E_{rn}(s) = 1 + \frac{k\omega' s}{s^2 + \omega_c s + \omega'^2} \tag{3.12}$$

## 3.4. EXPERIMENTAL VALIDATION

According to the analysis, the dual-loop GCF scheme is equivalent to the single-loop ICF scheme when the inner damping gain is set to $K_p$. As a result, similar to the single-loop ICF scheme, the dual-loop GCF scheme is stable when the resonance frequency is lower than the critical frequency. To prove it, an LCL-filtered grid-connected VSI system was built in the laboratory as shown in Figure 3-7. A detailed description about the experimental setup can be found in **J4**. Figure 3-8(a) shows the waveforms generated by changing the inner damping gain from $K_p$ to zero. The LCL-filter resonance frequency is 1.31 kHz, which is in the stable region of the single-loop ICF scheme while in the unstable region of the single-loop GCF scheme. It is noted from Figure 3-8(a) that, when the inner damping gain is $K_p$, the dual-loop GCF scheme is stable, because it is equivalent to the single-loop ICF scheme. In comparison, when the inner damping gain is changed to 0, the control system cannot be unstable any more since it becomes the single-loop GCF system. Similar result is shown in Figure 3-8(b) with the inner-loop gain changed from $K_p$ to $0.5K_p$. Due to the additional damping provided by the inner loop, the instability in Figure 3-8(b) is not as serious as that in Figure 3-8(a) where the inner-loop gain is changed to 0.

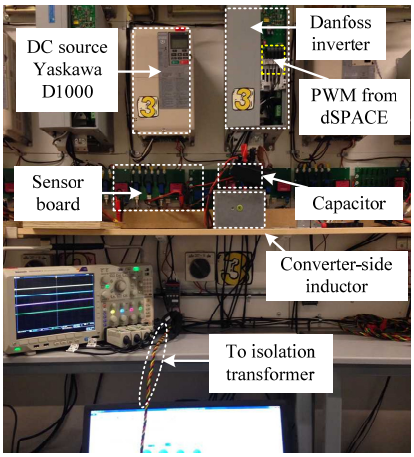


*Figure 3-7 Experimental setup[37].*

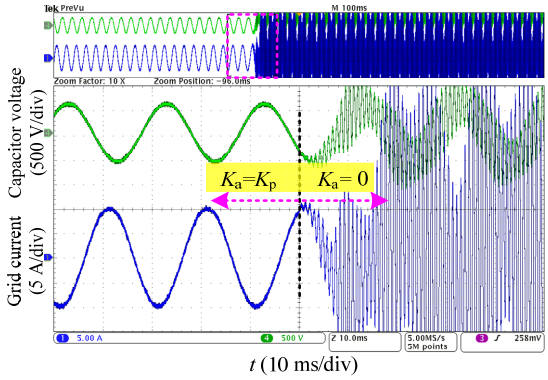


(a)

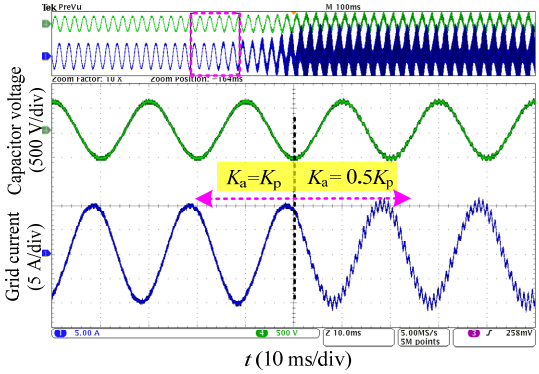


(b)

*Figure 3-8 Experimental results with the dual-loop GCF control, where the inner damping gain is changed from $K_p$ to (a) 0 and (b) 0.5$K_p$ [37].*

Next, the LCL-filter resonance frequency is increased to 1.85 kHz which is larger than the critical frequency of 1.67 kHz. If the inner damping gain is still $K_p$, the dual-loop GCF scheme cannot be stable anymore in principle. However, the parasitic resistance and the core loss of the inductor help to stabilize the system even though the resonance frequency is slightly larger than the crictical frequency, which can be seen from the steady-state waveforms in Figure 3-9(a). Nevertheless, in the dynamic state, the resonace is still activated due to the weak damping ability of the whole system, which can be found from Figure 3-9(a) when the current command is changed from 5 A to 10 A. In comparison, when the proposed SOGI-based time delay compensation is enabled, the resonance in the dynamic process is eliminated and the system shows enhanced damping ability as shown in Figure 3-9(b), which proves the effectiveness of the proposed method.

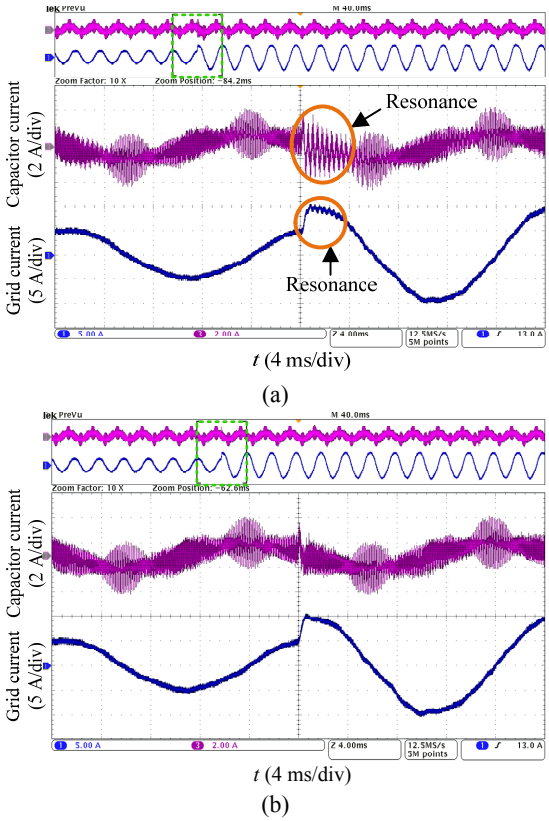


*Figure 3-9 Experimental results with the dual-loop GCF control (a) without and (b) with the proposed time delay compensation [37].*

## 3.5. SUMMARY

The relationship between the single-loop ICF scheme and dual-loop GCF scheme is investigated in this chapter. According to the result, the inner damping gain can be determined, which fixes the stable region of the dual-loop GCF scheme below the critical frequency regardless of the variation of LCL-filter parameters and grid impedance. Next, a SOGI-based time delay compensation approach is proposed to enhance the stability of the dual-loop GCF scheme, whose effectiveness is finally validated by experimental results.

# CHAPTER 4. HARMONIC MITIGATION OF LCL-FILTERED VSI WITH INVERTER CURRENT CONTROL [J6]

This chapter focuses on the harmonic mitigation of the LCL-filtered VSI as shown in Figure 4-1. It begins by investigating the sensitivity of the LCL-filtered VSI to the grid-voltage harmonics, especially when the inverter-side current is controlled. The limitations of the traditional harmonic mitigation strategies, such as the harmonic controllers and the grid-voltage feedforward schemes, are identified. Finally, a simple and effective control scheme for the LCL-filtered VSI with the inverter-side control is proposed to overcome the problems.

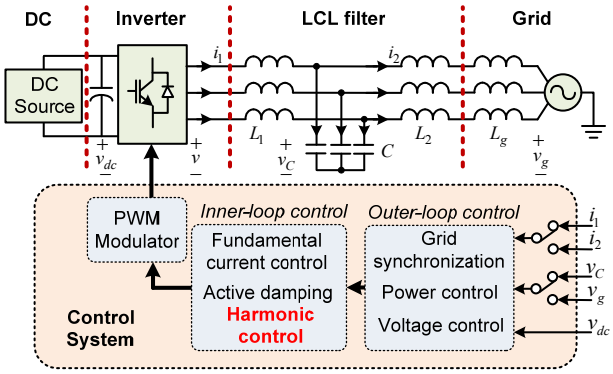


*Figure 4-1 Typical structure of the three-phase VSI system.*

## 4.1. HARMONIC ISSUES

Despite the excellent high-frequency attenuation performance of an LCL-filter, its low-inductance increases its susceptibility to low-order current distortions. Instead of increasing the inductance, it is much preferred to use control methods to deal with the low-order harmonics. The ICF control is mostly selected in industrial products, since current sensors have been installed in inverter-side for overcurrent protection and extra sensors for the control loop can be saved [27], [30], [45]–[47]. Besides, the ICF system has inherent damping characteristics [47], while for the GCF system, additional damping function has to be applied in the system in order to guarantee the stability of the system under weak grid conditions.

However, in an ICF control system, the grid current is regulated indirectly, which may suffer from severe distortion in face of grid-voltage harmonics, because the

harmonic current can freely flow through the capacitor without control [48], [49]. This issue can be well explained by the experimental result in Figure 4-2, where the inverter current is controlled to zero by the PR controller plus resonant HCs. However, it is noted that the grid current is seriously distorted by the grid-voltage harmonics, which flows into the filter capacitor without control.

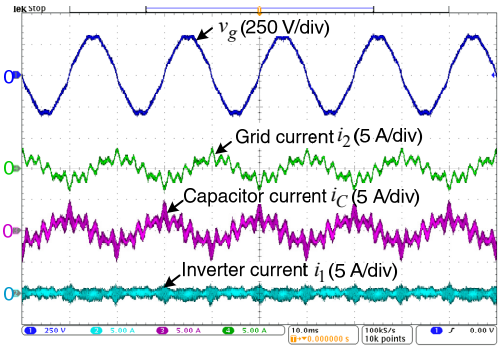


*Figure 4-2 Output current waveforms of the ICF-controlled VSI under distorted grid-voltage.*

## 4.2. TRADITIONAL SOLUTIONS

### 4.2.1. HARMONIC CONTROLLERS

Thanks to the infinite gains introduced by the HCs (resonant controller or repetitive controller), in an ICF system, the inverter current can be free of low-order distortion, no matter the harmonic sources are from the inverter-side or the grid-side. In case of inverter-side disturbance (e.g. dead-time effect), the grid current can also be free of distortion as long as the low-order harmonics have been eliminated from the inverter current before they flow into the grid-side inductor. However, in case of grid-voltage distortion, the resulting grid-current harmonics cannot be rejected by the HCs any more, due to the uncontrolled harmonic currents in the filter capacitor. To state the grid-current harmonic attenuation ability of the ICF control system explicitly, the grid harmonic impedance of the ICF control system is given by (4.1), which indicates the relationship of the grid voltage and the resulting grid current [27].

$$Z_g = \frac{v_g}{i_2} = \frac{\left(s^2 L_2 C + 1\right)\left(s^3 L_1 L_2' C + s\left(L_1 + L_2'\right) + G_c(s)e^{-sT_d}\left(s^2 L_2' C + 1\right)\right)}{1 + sC\left(s^3 L_1 L_2' C + s\left(L_1 + L_2'\right) + G_c(s)e^{-sT_d}\left(s^2 L_2' C + 1\right)\right)} \tag{4.1}$$

According to (4.1), at low and high frequencies, the harmonic impedance can be approximated by (4.2) and (4.3) respectively,

$$Z_{gLow} = \frac{v_g}{i_2} \approx K_p, \tag{4.2}$$

$$Z_{gHigh} = \frac{v_g}{i_2} \approx sL_2' . \tag{4.3}$$

It can be seen from (4.2) and (4.3) that the harmonic impedance shows resistive characteristic at low frequency and inductive characteristic at high frequency. The resistance is determined by $K_p$, while the inductance is determined by the grid-side inductor $L'_2$. Especially, at the frequencies where the HCs work, $G_c(s)$ becomes infinite and (4.1) can be approximated by:

$$Z_{gHarmonic} = \frac{v_g}{i_2} \approx sL_2' + \frac{1}{sC} . \tag{4.4}$$

These three characteristics can intuitively be illustrated with the help of the circuit model of the control system given in [50], where the principle of the PR controller is represented by a resistor and a bank of LC circuits as shown in Figure 4-3. The findings from this equivalent circuit can be concluded as follows:

- At very low frequency, the inductor impedance is very small and the capacitor impedance is very large, which is seen as a short circuit and an open circuit respectively. In this case, the current contributed by the grid voltage mainly flows in loop A, whose impedance is dominated by the resistance with the value of $K_p$.

- At very high frequency, the capacitor is seen as a short circuit, and thus the current contributed by grid voltage mainly flows in loop B, whose impedance is dominated by $L'_2$.

- At frequencies where the HCs work, the impedance of the LC circuits become infinite. Thus, the current contributed by the grid voltage mainly flows in loop B whose impedance is dominated by $L'_2$ and the filter capacitor $C$.

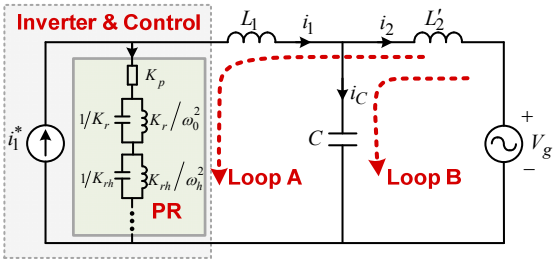


*Figure 4-3 Equivalent circuit of the LCL-filtered VSI with the inverter-side current controlled by a proportional-resonant controller plus resonant HCs.*

To illustrate these characteristics more exactly, *Figure 4-4* shows the Bode plot, which compares the harmonic impedances of the ICF control systems whose harmonic controllers are disabled and enabled respectively. The controllers are designed according to [51]. The fundamental resonant controllers of these two systems are both disabled in order to clearly distinguish their difference coming only from the harmonic controllers.

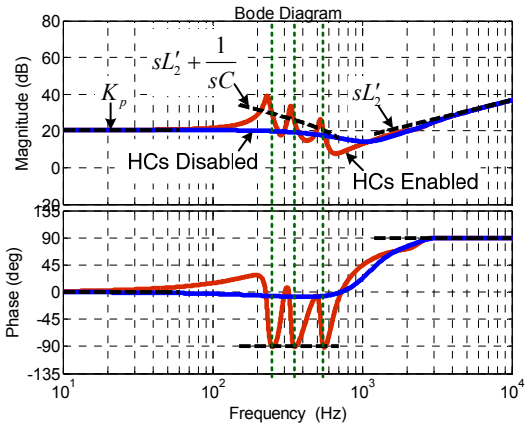


*Figure 4-4 Bode diagram of the grid harmonic impedance for the ICF control system when harmonic controllers are enabled and disabled.*

It can be observed from the Bode plot that around the working frequencies of the HCs, the harmonic impedance of the system is slightly larger than that when the HCs are disabled, because the current contributed by the grid voltage can flow both in loop A and loop B when the HCs are disabled, which has a lower impedance than loop B due to the parallel topology. It can be concluded that, although the HCs of the ICF control system cannot reject the grid-current harmonics completely, their existence help to attenuate the harmonics to some extent. However, the attenuation is quite limited, which is always below 40 dB in the provided case. Moreover, at the working frequencies of HCs, the impedance values are only determined by $L_2$ and $C$ (see (4.4) and *Figure 4-4*), since the grid-current harmonics only flow from $L_2$ to $C$ when the HCs are enabled. Therefore, the harmonic attenuation capability is fixed by the filter parameters and cannot be improved by designing the controller parameters. Unfortunately, in commercial products, in order to get a similar filtering performance, a comparative large capacitor is preferred instead of a large grid-side inductor in order to reduce the volume and cost of the filter stage. As a result, the harmonic impedance will be small according to (4.4).

### 4.2.2. GRID-VOLTAGE FEEDFORWARD

To cope with the harmonic issue of the ICF control system, the feedforward scheme, which has been used widely for the L-filtered VSI, has also been extensively

researched for the ICF-controlled LCL-filtered VSI [27], [30], [45]. A proportional grid-voltage feedforward strategy was applied in [30], which was said to have excellent harmonic-attenuation performance, since the LCL-filter was simply treated as an L filter by the authors. However, its effectiveness is deteriorated when the filter capacitor is considered. Instead of using the proportional feedforward, a transfer function was derived and inserted into the feedforward loop [45], aiming for eliminating an undesirable admittance effect. Unfortunately, the grid current can still be distorted by grid-voltage harmonics, since the feedforward term is the capacitor voltage rather than the grid voltage. In [27], an accurate feedforward function for grid voltage was derived, which can eliminate the influence of the grid voltage on the grid current completely. However, a second-order differentiator is required in order to synthesize the feedforward function, which is sensitive to noise and makes the method impractical. Although an alternative capacitor-current feedforward scheme was also given in [27] to overcome the drawback, it is still impractical due to the increased cost for capacitor-current measurement.

### 4.2.3. CAPACITOR-CURRENT FEEDFORWARD

In addition to the above two methods, another solution is to make the current reference contain the full harmonic information, which can be implemented by calculating the capacitor current from the capacitor voltage and then adding it to the reference. This idea was reported to be effective for the ICF control system with the novel D-Σ digital controller [46]. However, it is hardly used in the typical PR or PI controlled ICF system in literature, which may be attributed to the instability risk introduced by the feedforward loop. Specifically, since the modified system is equivalent to the GCF system, its stable region becomes the same with the GCF as well, which is ($f_s/6$, $f_s/2$) rather than (0, $f_s/6$). In this case, additional damping needs to be designed in order to ensure the system stability under weak grid condition. Detailed analysis of the problem was provided in **J6.**

## 4.3. PROPOSED HARMONIC MITIGATION STRATEGY

### 4.3.1. CONTROL STRUCTURE

To avoid the instability of the system with capacitor-current feedforward, a direct solution is to insert multiple band-pass filters into the feedforward loop, which only allows the predefined harmonics to pass. Despite its effectiveness, as the number of the harmonics to be attenuated increases, the computational burden increases as well. To solve the problem, a very simple scheme is proposed, which has the same computational effort but has a different feedforward position as shown in Figure 4-5.

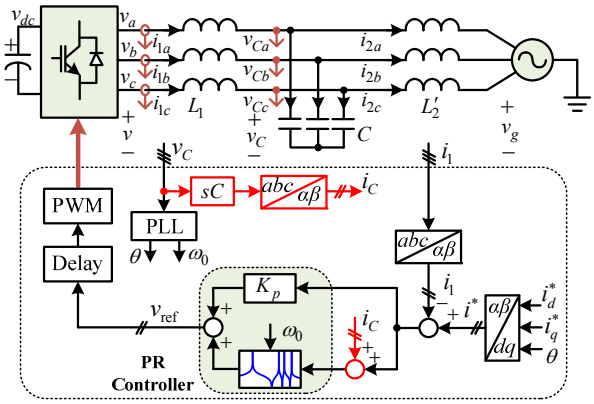


*Figure 4-5 Three-phase ICF-controlled LCL-filtered VSI with the proposed control.*

## 4.3.2. STABILITY AND HARMONIC IMPEDANCE ANALYSIS

In the proposed method, the capacitor current is only processed by the resonant controllers instead of the proportional controller. Since the stability of the control system is mainly determined by $K_p$, the added feedforward term will not influence the stable and unstable regions of the control system. To illustrate it, the root loci of the proposed system are plotted in Figure 4-6 with three resonance frequencies. It can be observed that the stable region of the proposed system is in agreement with the typical single-loop ICF control system despite an additional feedforward loop.

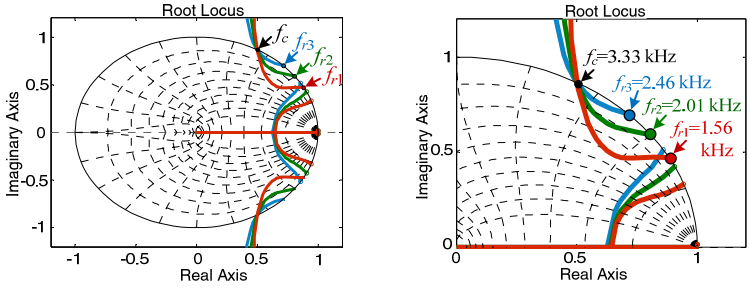


*Figure 4-6 Root loci of the proposed system when the LCL-filter resonance frequency is below the critical frequency, (a) full root loci (b) partially enlarged root loci.*

In terms of harmonic attenuation, the proposed scheme is, however, much superior to the single-loop ICF control system, as observed from the Bode plot in Figure 4-7, where the infinite impedance is obtained at the working frequencies of the HCs thanks to the grid harmonic information provided by the feedforward term. Looking back at Figure 4-5, it is interesting to find that the proposed scheme is actually a combination of an ICF control system and a GCF control system (the inverter current is controlled by the proportional controller, while the grid current is

controlled by the resonant controllers). That is the reason why the proposed scheme can inherit the stability characteristic of the single-loop ICF control system and the harmonic control capability of the single-loop GCF control system simultaneously.

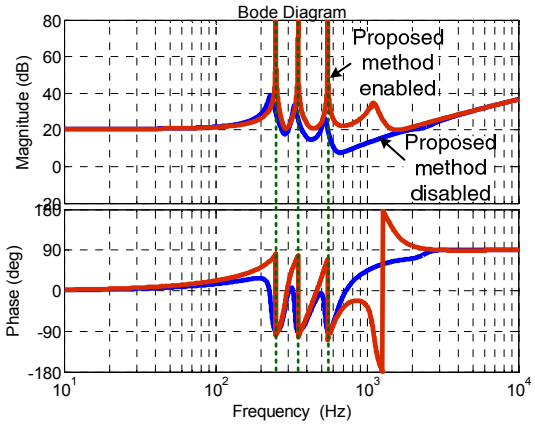


*Figure 4-7 Bode plot of the grid harmonic impedance when the proposed feedforward term is enabled and disabled.*

### 4.3.3. DIGITAL DIFFERENTIATOR DESIGN

To calculate the capacitor current, a differentiator is needed in the proposed method, which is difficult to be implemented accurately in a digital system. To overcome the drawback, the adjustable digital differentiator developed in [52] is applied in the proposed control system. The proposed control system is not so sensitive to the magnitude error of the differentiator, since the error can be eliminated by the integration characteristic of the resonant controllers. However, the sensitivity of the proposed method to the phase error is unknown, which should be investigated to ensure an accurate harmonic control. Detailed investigation was provided in **J6**.

### 4.3.4. CONTROLLER DESIGN

When the parameter of the LCL-filter is specified, stability of the system will mainly be determined by the proportional gain of the current controller. Considering that the proportional control branch of the system is the same with the typical single-loop ICF control system, the proportional gain can be designed similarly. Generally, for LCL-filtered VSI, the proportional gain $K_p$ of the current controller is designed using the same procedure for an L-filtered system. To illustrate it, the open-loop transfer function of the single-loop ICF control system is given by:

$$T_{il}(s) = K_p e^{-sT_d} G_p(s). \tag{4.5}$$

where $G_p(s)$ is the plant transfer function. For ICF and GCF control, it can be given by (4.6) and (4.7) respectively.

$$G_{pCCF} = \frac{i_1(s)}{v(s)} = \frac{s^2 L_2 C + 1}{s^3 L_1 L_2' C + s(L_1 + L_2')} \tag{4.6}$$

$$G_{pGCF} = \frac{i_2(s)}{v(s)} = \frac{1}{s^3 L_1 L_2' C + s(L_1 + L_2')}. \tag{4.7}$$

At low-frequency, (4.6) and (4.7) can both be reduced to:

$$G_p = \frac{1}{s(L_1 + L_2')}. \tag{4.8}$$

Thus, the phase response of (4.5) at low frequency is dominated by the inductor and the total time delay, whose phase contributions are $-\pi/2$ and $-\omega T_d$ respectively. For a specified phase margin $\Phi_m$, the crossover frequency can be calculated by:

$$\omega_c = \frac{\pi/2 - \Phi_m}{T_d}. \tag{4.9}$$

The proportional gain can then be calculated by setting the open-loop gain to be unity at the crossover frequency, which is given by:

$$K_p = \omega_c (L_1 + L_2'). \tag{4.10}$$

Since the approximation of an L filter is only reasonable at low frequency, this method makes sense for the system whose LCL-filter frequency is far from the bandwidth, such as the traditional GCF control system [39], or the ICF system with the LCL-filter resonance frequency designed beyond the Nyquist frequency [11].

However, this design method is not proper for parameter design of the typical ICF control system, whose LCL-filter resonance frequency is designed below the critical frequency for stability concern, where the plant cannot be approximated as an L-filter anymore. Figure 4-8 shows the open-loop Bode plot of an ICF control system. It is observed that three 0-dB crossing frequencies always exist, due to the resonance peak and the anti-resonance peak of the magnitude response. Among these three frequencies, the largest one relates to the smallest phase margin, which should be selected for the $K_p$ design.

Before designing $K_p$, the crossover frequency should first be calculated according to a given phase margin. It is noted that, between the antiresonance frequency and the resonance frequency, the phase jump leads to a short duration of larger phase margin, after which, the phase becomes decided by the inductor and the time-delay

again. Therefore, it is reasonable that, (4.9) can still be used for the crossover frequency calculation, since it is a stricter constraint. The proportional gain $K_p$ can next be calculated by setting the open-loop gain to be unity at the crossover frequency. However, (4.6) cannot be simplified to (4.8) near the LCL-filter resonance frequency anymore, which means (4.10) will be inaccurate when used for $K_p$ calculation. To avoid the problem, the magnitude-frequency equation should be derived from (4.6), with which, $K_p$ can be designed by:

$$K_p = \left| \frac{-\omega_c^3 L_1 L_2' C + \omega_c \left( L_1 + L_2' \right)}{-\omega_c^2 L_2' C + 1} \right| . \tag{4.11}$$

As for the gain of the resonant controller, it can be designed by ensuring that its phase contribution is small at the crossover frequency [39], [51], i.e.,

$$K_r = \frac{K_p \omega_c}{20} . \tag{4.12}$$

To ensure the system stability and a fast dynamic response, the phase margin is set to 40° in the target system, and the sampling frequency is 20 kHz in the setup, which results in the crossover frequency of 1.85 kHz. The Bode plot of the open-loop transfer function derived from the proposed control structure in Figure 4-5 is shown Figure 4-8. It can be seen that the phase margin is 40.4° and the crossover frequency is 1.84 kHz, both of which are very close to the designed values.

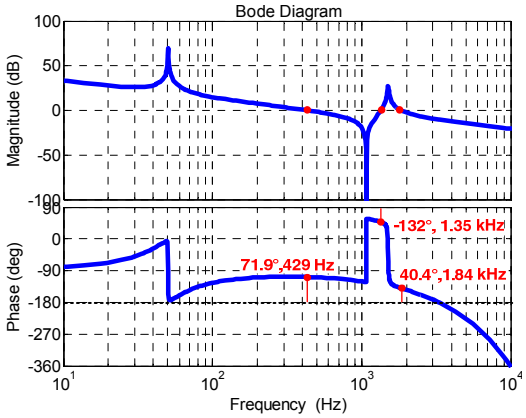


*Figure 4-8 Bode plot of the proposed control system with a 40° designed phase margin.*

### 4.3.5. EXPERIMENTAL VALIDATION

Figure 4-9 shows the experimental setup in the lab to validate the effectiveness of the proposed method. The parameters of the system can be found in **J6**. Figure 4-10(a) shows the waveforms of the inverter current and the grid current under an

ideal grid condition. Thanks to the HCs, the THD of the grid current is only 0.6 % under ideal grid condition, which is much lower than the 5 % required by the grid standards.

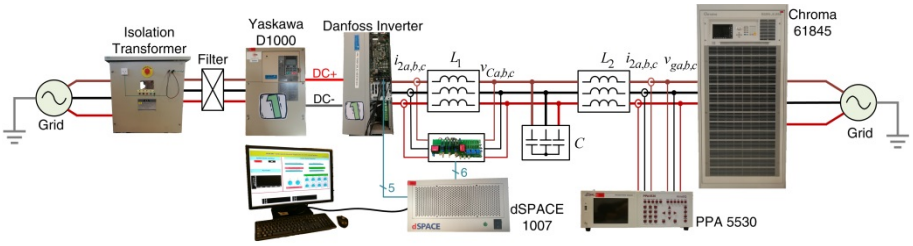


*Figure 4-9 Experimental setup.*

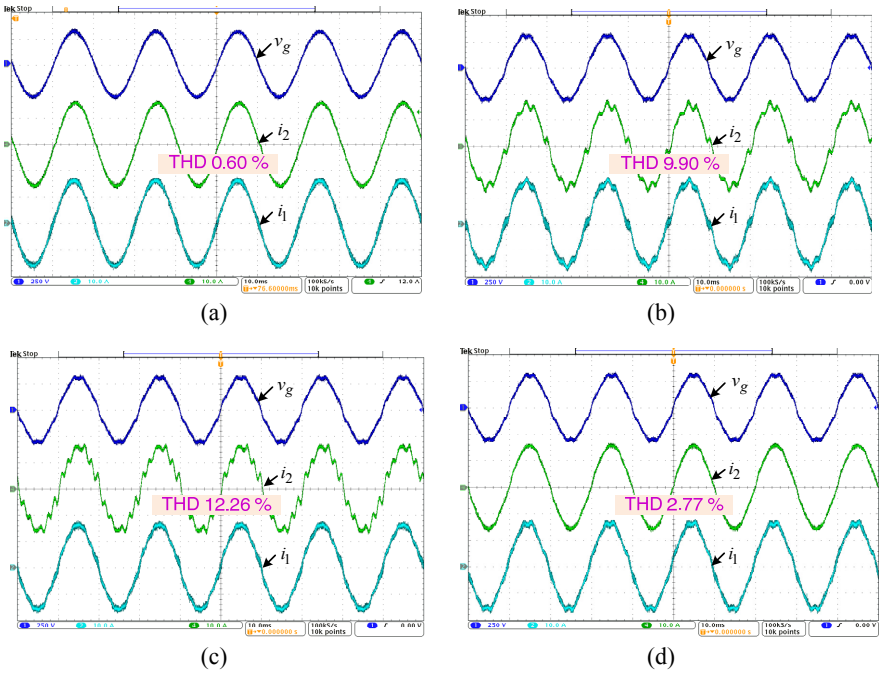


(a) (b) (c) (d)

*Figure 4-10 Experimental waveforms of the grid current and inverter current (a) with HCs under ideal grid, (b) without HCs under distorted grid, (c) with HCs under distorted grid, and (d) with the proposed control under distorted grid.*

In comparison, the grid voltage output from the simulator is set to be distorted by low-order harmonics (5th, 7th, and 11th, THD ≈4.9 %) in Figure 4-10(b). It is noted that both the grid current and the inverter current become seriously distorted without HCs. Especially, a THD of 9.9 % is observed in the grid current in Figure 4-10(b),

which exceeds 5 % required by the grid standard, showing the severe influence of the grid-voltage harmonics on the grid-current quality.

In order to mitigate these harmonics, the conventional resonant HCs tuned at the 5th, 7th, and 11th harmonic frequencies are enabled in Figure 4-10(c). As a result, the inverter current becomes less distorted due to the infinite harmonic impedance provided by the HCs. However, despite the effectiveness of the HCs on the inverter current harmonic rejection, they fail to mitigate the grid-current distortions, which become even more serious with the THD increased to 12.26 % in Figure 4-10(c).

The proposed scheme is then enabled in Figure 4-10(d), where the capacitor current is calculated from the GI-based differentiator and fed forward to the input of the resonant controllers. Since the capacitor current contains the harmonic information, the proposed control makes sure that all harmonics are produced from the inverter side rather than the grid-side. As a result, the grid current can be free of distortion in principle. Obviously, it is observed from Figure 4-10(d) that, with the proposed method, the grid-current waveform becomes much less distorted, which has only a THD of 2.77 % and complies well with the grid standard. The experimental results are in agreement with the theoretical analysis and the simulation results. Hence, the effectiveness of the proposed method under grid voltage distortion is validated.

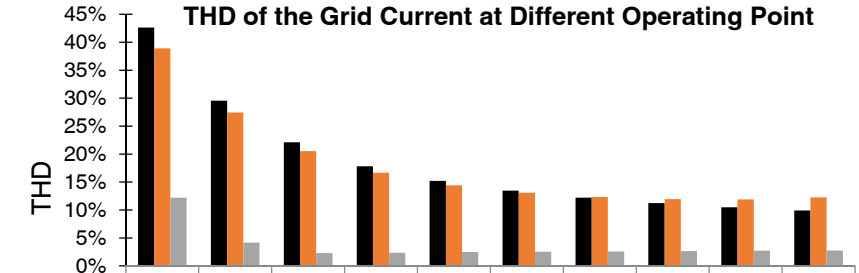


| | 10% | 20% | 30% | 40% | 50% | 60% | 70% | 80% | 90% | 100% |
|---|---|---|---|---|---|---|---|---|---|---|
| W/O HCs | 42,63% | 29,55% | 22,10% | 17,82% | 15,21% | 13,47% | 12,19% | 11,22% | 10,49% | 9,90% |
| With HCs | 38,91% | 27,42% | 20,52% | 16,68% | 14,42% | 13,09% | 12,32% | 11,94% | 11,90% | 12,26% |
| Proposed | 12,21% | 4,16% | 2,30% | 2,36% | 2,51% | 2,53% | 2,60% | 2,65% | 2,72% | 2,77% |

*Figure 4-11 THD of the grid current $i_2$ for three different control systems at different operating point.*

To give a more comprehensive comparison, for the three control schemes used in Figure 4-10, the THD of the grid current are measured at different operating point: from 10 % to 100 % of the rated power. The grid voltage distortion is the same with that in the previous experiments. The results are recorded in Figure 4-11 and shown by the bar chart, where it can be observed that the proposed method has the lowest THD at all operating points among the three control schemes. Specifically, above

30 % of the rated power, the proposed method can guarantee the THD to always be lower than 3 %, while for the other two control systems, the THD are almost all larger than 10 %. Although the relative THD of the proposed method at 10 % of the rated power is 12.21 %, its corresponding absolute value becomes 1.2 % which is still lower than the 5 % required by the grid standard. Besides, it is noted that, above 60 % of the rated power, the use of HCs even worsens the grid current quality as a larger THD is observed compared with the system without HCs.

## 4.4. SUMMARY

This chapter proposes a very simple and effective grid-current harmonic mitigation strategy for the LCL-filtered VSI using ICF control, which makes the inverter possible to inject high-quality current to the grid even under grid voltage distortion. The proposed method is equivalent to a control system using a proportional controller for the inverter current control, while resonant controllers for the grid current control. As a result, the proposed system inherits the superior stability characteristic of the ICF control system and the excellent grid-current harmonic controllability of the GCF control system simultaneously. To implement the control algorithm, a differentiator realized by the non-ideal GI is employed to avoid extra current sensors. Eventually, the experimental results are presented to verify the effectiveness of the proposed method.

# CHAPTER 5. GRID SYNCHRONIZATION OF LCL-FILTERED VSI BASED ON SECOND-ORDER GENERALIZED INTEGRATOR [J5]

This chapter focuses on the performance improvement of the SOGI based grid synchronization scheme. To begin with, a comprehensive review of the SOGI-based filters from a first-order system perspective and a circuit perspective is presented, through which, the principle of the SOGI-based filters can be intuitively understood. Furthermore, two improved SOGI-QSGs are proposed. The first one has a fourth-order transfer function and thus has enhanced filtering performance at both low- and high-frequency. The second one is a second-order system, which is similar to the structure of the basic SOGI-QSG, while the proposed one can realize accurate parameter design based on a desired transient performance.

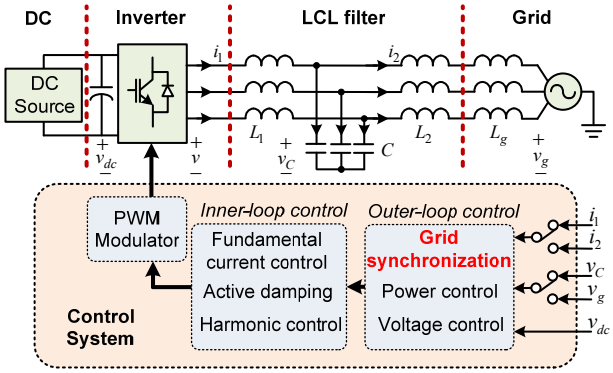


*Figure 5-1 Typical structure of the three-phase VSI system.*

## 5.1. INTUITIVE UNDERSTANDING OF SOGI-BASED FILTERS

### 5.1.1. DEVELOPMENT TIMELINE OF THE SOGI-BASED QUADRATURE SIGNAL GENERATOR (SOGI-QSG) AND SEQUENCE FILTER

Figure 5-2(a) shows the development timeline of the SOGI-QSG, which was early employed in [53] and [54] for the instantaneous power calculation in a single-phase system. It was then used as a prefilter of PLL to implement the grid synchronization under a grid distortion condition [55], [56]. Further, the authors of [57] developed a Frequency-Locked Loop (FLL) based on SOGI-QSG and the scheme coincides with

the Adaptive Notch Filter (ANF) proposed in [58]. The ANF was developed based on the research of [59], [60], and [61]. Later, the multiple SOGI-FLL was proposed for harmonic extraction in [62]–[64], which can also be realized by the ANF in [65]–[67]. Besides these applications, the SOGI-QSG has also been used in many other fields [41], [68]–[73], reflecting its importance in industrial applications.

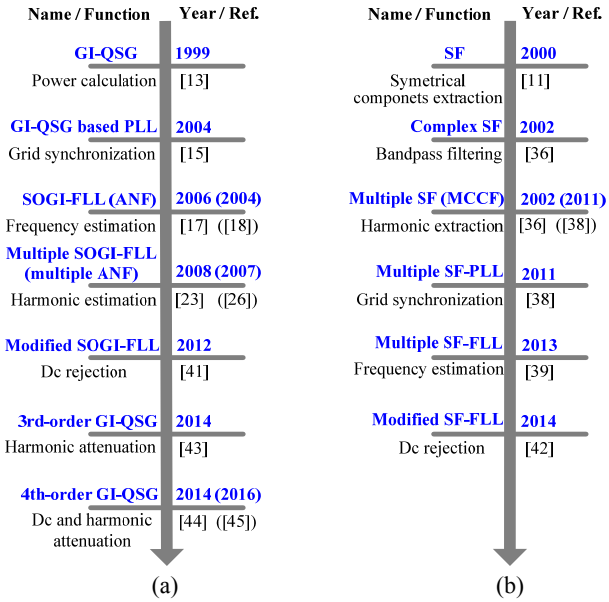


*Figure 5-2 Development timeline of (a) SOGI-QSG based filters and (b) Sequence Filter (SF) based filters .*

The SOGI-QSG block can be looked as a summation of two complex filters which when used to build closed-loop system lead to the Sequence Filters (SF) for either positive-sequence or negative-sequence component extraction. The development timeline of the SF is very similar to the SOGI-QSG, as in Figure 5-2(b). Despite the wide applications of SOGI-QSG and SF, their structures and principle illustrations are complicated, making them difficult to be distinguished and applied properly in a short time. To overcome the drawback, two novel approaches are presented to re-investigate these filters. One is from the First-Order System (FOS) perspective and the other is from the circuit perspective.

## 5.1.2. INTUITIVE UNDERSTANDING OF THE SOGI-QSG FROM A FIRST-ORDER SYSTEM PERSPECTIVE

### 5.1.2.1 Three first-order systems

*1) Standard First-Order System (FOS)*

Figure 5-3(a) shows the structure of the standard FOS which is built by a pure integrator. The output of the FOS is able to track the dc input signal thanks to the infinite gain of pure integrator. The step response of the FOS is shown in Figure 5-3(b), where it is noted that the output converges to the input gradually, verifying the dc-signal tracking capability of the FOS. The error between the input and output of the FOS is 1.83% at the time $4/k$ which is defined as the settling time $t_s$ in [74].

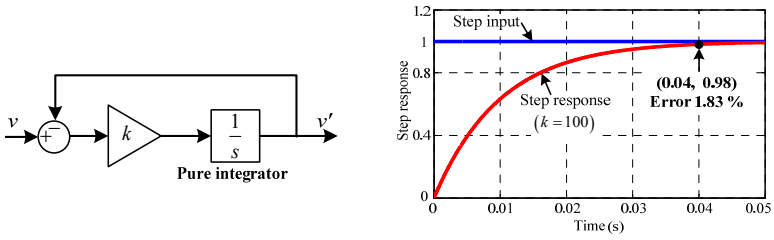


*Figure 5-3 Block diagram (a) and step response (b) of the First-Order System (FOS) [75].*

*2) Pure Sinusoidal Integrator and Sinusoidal FOS*

The FOS, however, cannot be used to track the sinusoidal signal, because the pure integrator has a finite gain at non-zero frequencies. This problem can be solved by shifting the infinite gain of the pure integrator to the frequency of the sinusoidal signal, which then results in the structure of the sinusoidal FOS (SFOS) shown in Figure 5-4(a). The response of the SFOS is plotted in Figure 5-4(b), where it can be seen that the amplitude response of the SFOS follows that of the FOS all the time, i.e. the SFOS and the FOS share the same settling time $t_s$.

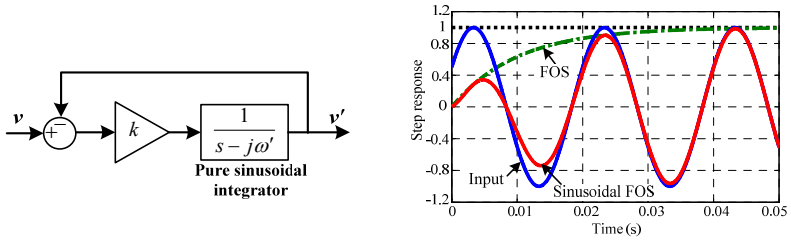


*Figure 5-4 Block diagram (a) and step response (b) of the Sinusoidal FOS [75].*

*3) Symmetrical Sinusoidal Integrator and Symmetrical Sinusoidal FOS*

The input of SFOS should be a complex vector, which is difficult to get in a single-phase system. To solve this problem, a positive-sequence Pure Sinusoidal Integrator (PSI) and a negative-sequence PSI are combined as a Symmetrical Sinusoidal Integrator (SSI) which avoid the implementation of the complex constant $j$. To

investigate the effectiveness of the resulting Symmetrical SFOS (SSFOS) in Figure 5-5(a) for sinusoidal signal tracking, its response is shown in Figure 5-5(b), which is very close to that of the SFOS. Although the SSFOS has a second-order transfer function, it is denoted as "first order" since its magnitude response has an FOS characteristic.

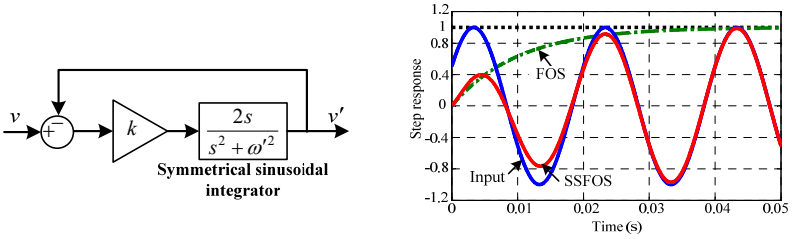


(a) (b)

*Figure 5-5 Block diagram (a) and step response (b) of the Symmetrical Sinusoidal FOS [75].*

### 5.1.2.2 Re-evaluation of SOGI based filters from an FOS and a circuit perspective

The above three systems (FOS, SFOS, and SSFOS) can be employed to illustrate many SOGI based filters, which not only provides a generalized way to investigate their principles but also simplifies their parameter design procedures. Hereinafter, three filters are explained from the FOS and circuit perspective as examples, while more examples can be found in **J5**.

*1) SOGI-QSG*

Figure 5-6(a) shows the structure of SOGI-QSG whose transfer functions are given by (2.21) and (5.1), where the former is a band-pass filter with zero phase-shift and unity gain at $\omega'$ and the latter is a low-pass filter with 90° phase shift and unity gain at $\omega'$ [33]. The SOGI-QSG is essentially an SSFOS. To illustrate it, transfer function of the SSI is re-written as (5.2) which can be seen as a closed-loop transfer function of a system with a gain $\omega'/s$ in both its feedback path and forward path. Based on this understanding, the SSFOS can be described by the structure in Figure 5-6(b). It is interesting to note that the structures of the SOGI-QSG and the SSFOS are essentially the same when $k'$ is set to $2k/\omega'$. Therefore, the parameter of SOGI-QSG can be designed according to that of the SSFOS.

$$Q(s)=\frac{qv'(s)}{v(s)}=\frac{k'\omega'^2}{s^2+k'\omega's+\omega'^2}. \tag{5.1}$$

$$SSI(s)=\frac{2s}{s^2+\omega'^2}=\frac{2}{\omega'}\frac{\omega'/s}{1+\omega'^2/s^2}. \tag{5.2}$$

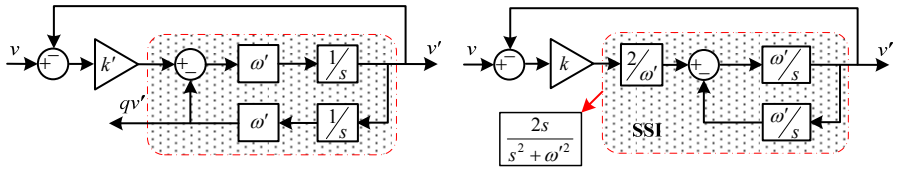


*Figure 5-6 Block diagram of (a) the SOGI-QSG and (b) the SSFOS [75].*

The principle of SOGI-QSG can be explained by the circuit in Figure 5-7, where $Z_b$ is the base impedance. In Figure 5-6(a), if $k'$ is looked as the admittance, the error signal $v - v'$ will be the voltage across the resistor with the value $Z_b/k$. The generated current then flows into the shaded part of Figure 5-6(a), where the two integrators are equivalent to an inductor and a capacitor connected in parallel. In this case, $v'$ is the voltage across the capacitor and inductor, while $qv'$ is the current in the inductor. Parallel resonance can hence be generated between the inductor and capacitor, which leads to two in-quadrature signals $i_L$ ($qv'$) and $u_c$ ($v'$) in steady state. The principle of the SOGI-QSG can thus be intuitively understood.

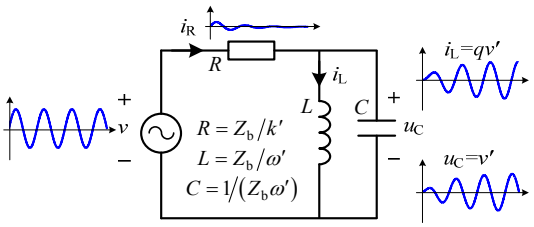


*Figure 5-7 Equivalent circuit of the SOGI-QSG.*

*2) Modified SOGI-QSG*

The basic SOGI-QSG structure is sensitive to the dc component in the input signal [34], [35], since $qv'$ is the low-pass-filter version of the input. To solve the problem, the authors of [35] proposed a modified SOGI-QSG structure shown in Figure 5-8(a), where an extra integrator was added into the basic SOGI-QSG to extract the input dc component. Finally, the outputs $v'$ and $qv'$ can be free of dc influence. The modified SOGI-QSG is actually a combination of an FOS and an SSFOS with a common feedback shown in Figure 5-8(b), which makes the parameter design of the modified SOGI-QSG clear. Moreover, Figure 5-9 shows the equivalent circuit of the modified SOGI-QSG, where one extra capacitor is added into the circuit of SOGI-QSG for representing the additional integrator. It is evident that any residual offset from the input signal can be prevented by the capacitor. The working principle of the modified SOGI-QSG can thus be explained intuitively.

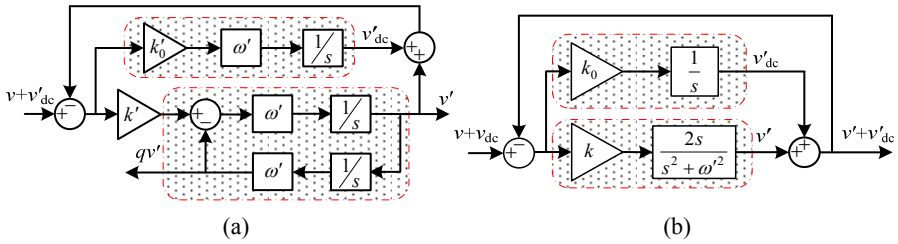


*Figure 5-8 Block diagram of the (a) modified SOGI-QSG and (b) combined FOS [75].*

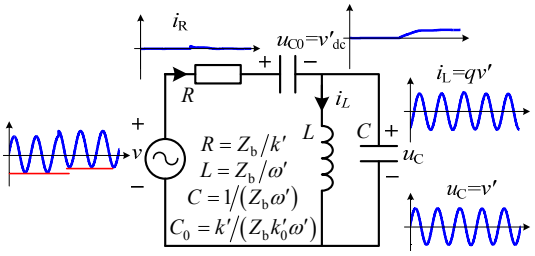


*Figure 5-9 Equivalent circuit of the modified SOGI-QSG.*

### *3) Sequence Filter*

The SF was presented in [76] for extracting either positive-sequence or negative-sequence component, whose structure can be found in Figure 5-10(a). The other structure called Complex-Coefficient Filter (CCF) was proposed in [77] to realize the same function, whose structure is shown in Figure 5-10(b). Both of these two structures are equivalent to the SFOS since both of them are built by a sinusoidal integrator as seen from (5.3) and (5.4). Their equivalent circuit is shown in Figure 5-11, which contains two sub-circuits coupled with each other through two voltage-controlled current sources.

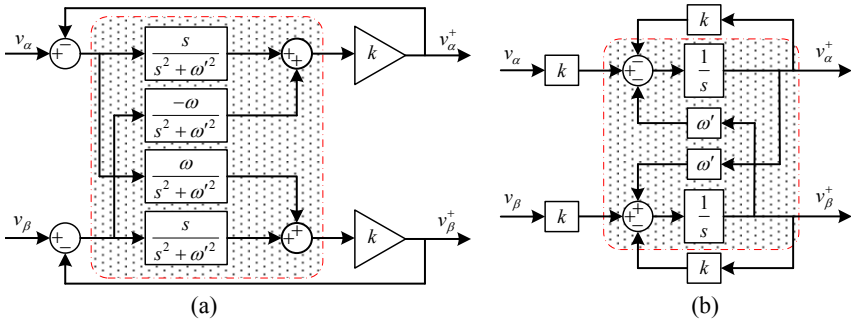


*Figure 5-10 Block diagrams of (a) the sequence filter [78] and (b) the complex-coefficient filter [77].*

$$SI(s)=\frac{1}{s-j\omega'}=\frac{s+j\omega'}{s^2+\omega'^2}=\frac{s}{s^2+\omega'^2}+j\frac{\omega'}{s^2+\omega'^2}\,. \tag{5.3}$$

$$SI(s)=\frac{1}{s-j\omega'}=\frac{1/s}{1-j\omega'/s}\,. \tag{5.4}$$

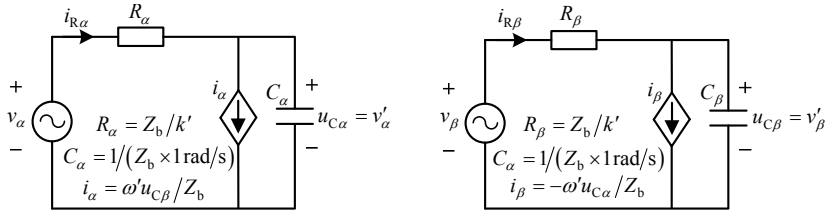


*Figure 5-11 Equivalent circuit of the SF.*

## 5.2. PROPOSED SO-SOGI-FLL WITH ENHANCED HARMONIC ATTENUATION

The FOS concept also provides convenience for developing new structures with improved performances. For example, in order to get a strong filtering performance, the SOGI-QSG and SF based filters can be modified to ‘‘second-order’’ systems whose structures can be derived by referring to the relationship between the standard FOS and the standard SOS. To explain it, an example is given as follows.

### 5.2.1. STANDARD SECOND-ORDER SYSTEM

To begin with, (5.5) shows the closed-loop transfer function of the standard SOS, where $\omega_n$ and $\zeta$ are the undamped natural frequency and the damping ratio of the SOS [74]. Its block diagram is next shown in Figure 5-12(a), where it is noted that the open-loop transfer function is composed by a pure integrator and a first-order inertia element. Since the first-order inertia element can be seen as an FOS, the structure of the SOS can thus be updated to the block diagram in Figure 5-12(b).

$$S(s)=\frac{\omega_n^2}{\left(s^2+2\zeta\omega_n s+\omega_n^2\right)} \tag{5.5}$$

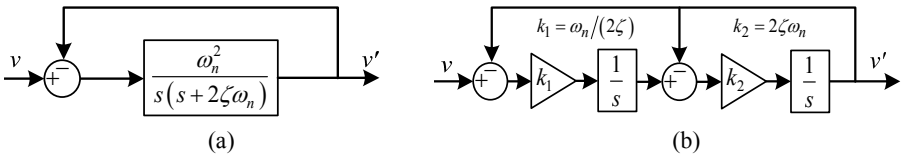


*Figure 5-12 Block diagrams of the SOS, (a) block diagram implemented with open-loop transfer function, and (b) block diagram implemented with two pure integrators [75].*

## 5.2.2. STRUCTURE DERIVATION OF THE PROPOSED SO-SOGI-FLL

The difference between the FOS in Figure 5-3 and the SSFOS in Figure 5-5 is their integrators. For the SOS in Figure 5-12(b), when the two integrators are replaced by two PSIs, the proposed SO-SOGI-QSG can be obtained. A more detailed structure is next shown in Figure 5-14 when the transfer functions of the PSIs are realized by block diagrams. Besides, an FLL block is added in order to make the algorithm frequency-adaptive. Although the SO-SOGI-QSG is actually a fourth-order function, it is named as a "second order" since it is derived from the standard SOS.

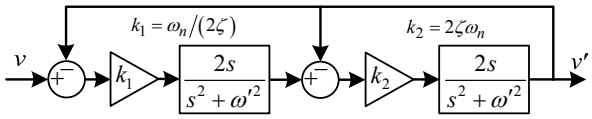


*Figure 5-13 Structure of SO-SOGI-QSG implemented with transfer functions [75].*

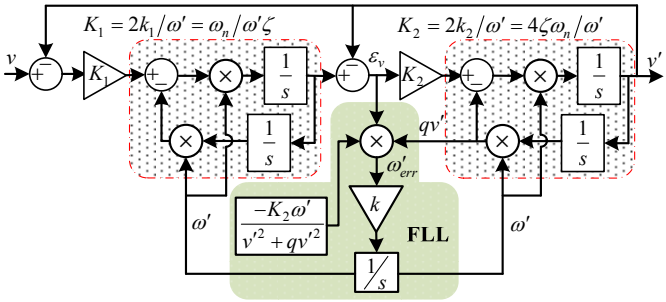


*Figure 5-14 Structure of SO-SOGI-FLL implemented with ideal integrators [75].*

The characteristic of the SO-SOGI-QSG is then investigated by first deriving its open-loop transfer function from Figure 5-14 as

$$O(s) = \frac{K_1 K_2 \omega'^2 s^2}{\left(s^2 + K_2\omega' s + \omega'^2\right)\left(s^2 + \omega'^2\right)} \tag{5.6}$$

The transfer functions for relating the input $v$ and the two outputs can be given by

$$D_s(s) = \frac{v'(s)}{v(s)} = \frac{O(s)}{1+O(s)} = \frac{K_1 K_2 \omega'^2 s^2}{\left(s^2 + K_2\omega' s + \omega'^2\right)\left(s^2 + \omega'^2\right) + K_1 K_2 \omega'^2 s^2} \tag{5.7}$$

$$Q_s(s) = \frac{qv'(s)}{v(s)} = D_s \frac{\omega'}{s} = \frac{K_1 K_2 \omega'^3 s}{\left(s^2 + K_2\omega' s + \omega'^2\right)\left(s^2 + \omega'^2\right) + K_1 K_2 \omega'^2 s^2} \tag{5.8}$$

To evaluate the performance of the SO-SOGI-QSG, the Bode plots of (5.7) and (5.8) are given in Figure 5-15(a) and Figure 5-15(b), which are compared with the method in [35] and the basic SOGI-QSG. The same comparison has also been organized in Figure 5-16(a) and Figure 5-16(b) for the Bode diagrams from [79]. To be fair, the parameters of these methods are set to ensure the same settling time. It can be seen that the SO-SOGI-QSG has the most excellent attenuation above and below $\omega'$.

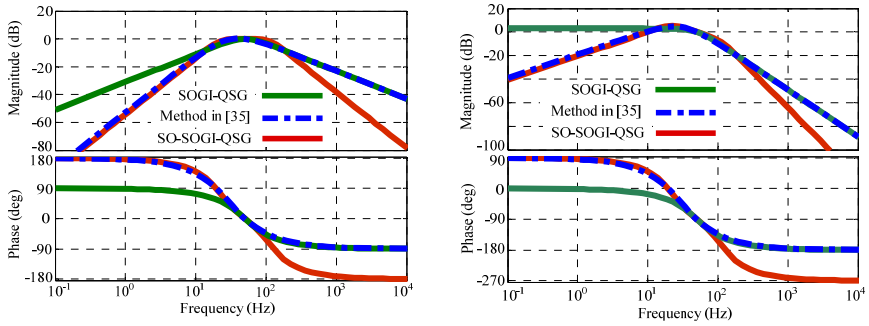


*Figure 5-15 Bode diagrams plotted with method from* [35]*, proposed SO-SOGI-QSG, and basic SOGI-QSG for relating (a) $v'$ to $v$, and (b) $qv'$ to $v$ [80].*

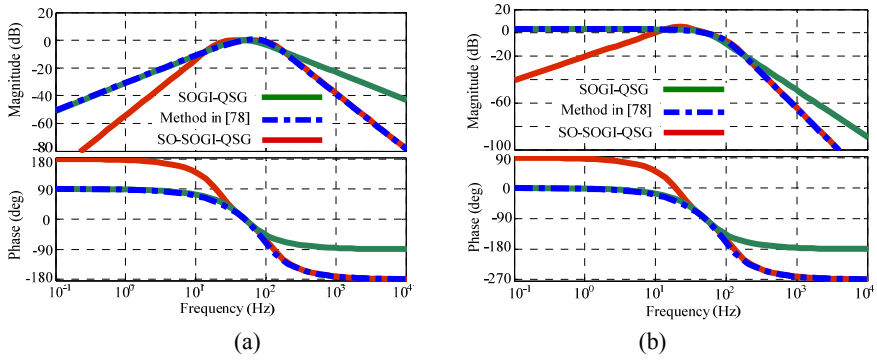


*Figure 5-16 Bode diagrams plotted with method from [79], proposed SO-SOGI-QSG, and basic SOGI-QSG for relating (a) $v'$ to $v$, and (b) $qv'$ to $v$ [80].*

### 5.2.3. EXPERIMENTAL VALIDATION

The effectiveness of SO-SOGI-QSG is verified by the experimental results and shown in Figure 5-17. The grid voltage contains the $5^{th}$, $7^{th}$ and $11^{th}$ harmonics and dc offset, which is processed by the SOGI-QSG, the algorithms in [35] and [79], and the SO-SOGI-QSG. It is noted that the $v'$ output of SOGI-QSG is distorted and its $qv'$ output contains an obvious dc offset. Although the dc offset is rejected in both $v'$ and $qv'$ of the method in [35], its $v'$ output is distorted like SOGI-QSG. As for the

method in [79], a smoother $v'$ is observed than that produced by SOGI-QSG. However, the dc offset exists in $qv'$. The results obtained from SO-SOGI-QSG show the best performance, for which $v'$ has the lowest distortion and the dc offset is rejected from $qv'$.

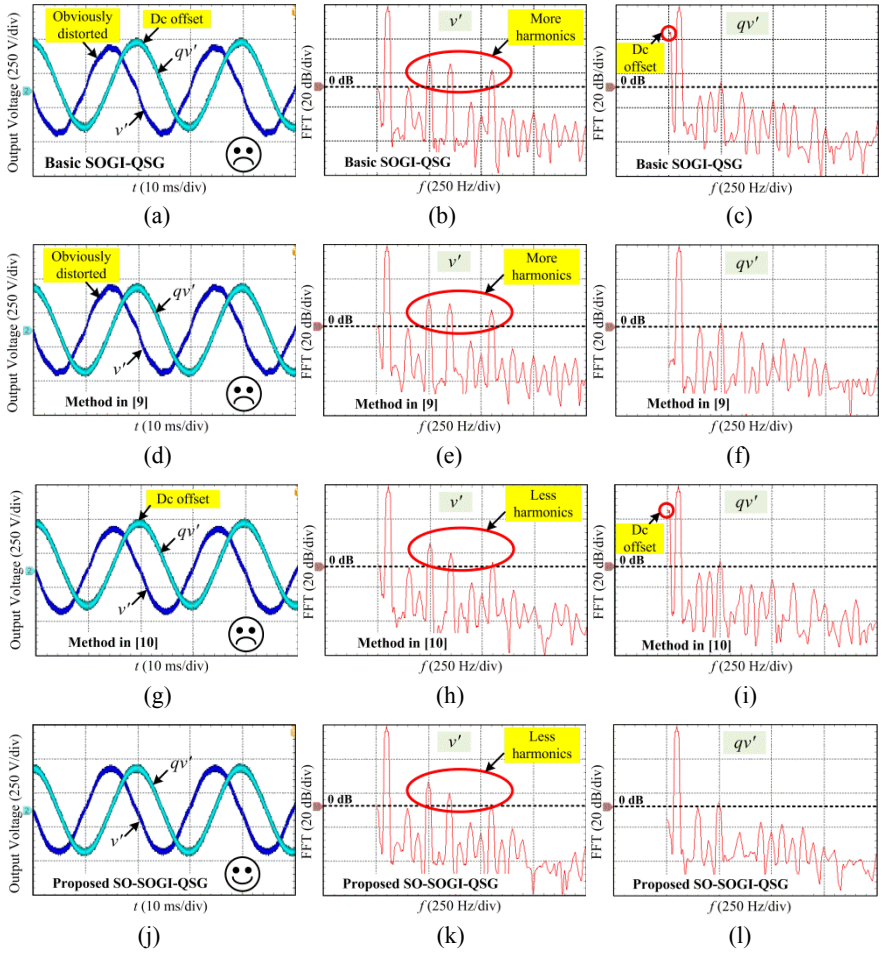


*Figure 5-17 Experimental results obtained with SOGI-QSG from (a) to (c), method in [35] from (d) to (f), method in [79] from (g) to (i), and SO-SOGI-QSG from (j) to (l) [80].*

## 5.3. PROPOSED ACCURATE-MAGNITUDE INTEGRATOR BASED QUADRATURE SIGNAL GENERATOR (AMI-QSG) WITH ACCURATE RESPONSE DESIGN

Block diagram of the SOGI-QSG is shown in Figure 5-6(a), where the parameter $k'$ determines the settling time of the QSG and thus should be designed properly in

order to ensure a fast and stable response. Generally, the principle of the SOGI-QSG can be understood from either a filter perspective or a first-order feedback system perspective, which correspondingly lead to two parameter design approaches.

From a filter perspective, the structure of SOGI-QSG can be seen as a combination of two filters: one is a band-pass filter relating to its in-phase output $v'$ and the other is a low-pass filter relating to its quadrature output $qv'$. Both of these two filters possess second-order transfer functions and thus the dynamic response of the SOGI-QSG can be designed by referring to a standard SOS, whose settling time is defined as the time when its output takes to get and stay within 2% of the final value [81]. This design rule is simple and straightforward and thus has been adopted without a doubt for the parameter design of the SOGI-QSG in most existing papers. However, different from the standard SOS, the effective input of the SOGI-QSG is a sinusoidal signal rather than a dc signal, which possesses three variables (frequency, phase, and magnitude) at the same time. Consequently, the settling time is not clear since it cannot tell which variable the designed response time refers to.

Alternatively, the SOGI-QSG can be understood from a FOS perspective, where the inner SOGI block shows magnitude-integration characteristic to the input sinusoidal signal when its working frequency is tuned to the input signal frequency. As mentioned previously, this working principle is in agreement with the dc-integration characteristic of the pure integrator which is the core building block of an FOS for dc-signal tracking. Consequently, the magnitude response of the SOGI-QSG to a sinusoidal input signal coincides with that of the FOS to a dc input signal. Therefore, the dynamic response of the SOGI-QSG can be designed easily by referring to that of the FOS. However, theoretical analysis shows that this design rule is only effective when the settling time of the SOGI-QSG is large enough, which yet becomes inaccurate when a fast response of the SOGI-QSG is required. Unfortunately, in most power converter applications, the settling time of the SOGI-QSG is expected to be around (or even less than) one fundamental period, making this design rule lose its effectiveness.

### 5.3.1. PROBLEM ANALYSIS OF THE SOGI-QSG

As mentioned, the pure integrator of an FOS has an infinite gain at zero frequency and thus can achieve dc signal tracking. Different from the pure integrator, the GI is combined by two complex integrators (see (5.9)), which leads to two infinite gains at both the positive and the negative frequency. Especially, if the feedback system is built by a complex integrator, the tracking characteristic (see (5.10)) will be accurately consistent with that of the FOS. However, for the SOGI-QSG with a sinusoidal input signal, only one complex integrator in (5.9) works for signal tracking, while the other one disturbs the tracking process which leads to a different dynamic response of the system compared with the FOS. The influence is negligible when the dynamic response of the system is slow enough. However, when the

required settling time is very small, the response of the SOGI-QSG will become different from that of the FOS. To explain this issue explicitly, the response of the SOGI-QSG to a sinusoidal input signal $v(t) = A\sin(\omega t+\varphi)$ is derived.

$$GI(s) = \frac{2s}{s^2+\omega'^2} = \frac{1}{s-j\omega'} + \frac{1}{s+j\omega'} \tag{5.9}$$

$$v'(t) = A\left(1-e^{-kt}\right)\sin\left(\omega t+\varphi\right) \tag{5.10}$$

To begin with, the Laplace transform of the sinusoidal signal can be given by:

$$v(s) = \frac{A\omega\cos\varphi}{s^2+\omega^2} + \frac{As\sin\varphi}{s^2+\omega^2}. \tag{5.11}$$

The Laplace transform of the output of SOGI-QSG can be derived by multiplying (5.11) with (2.21) ($v'(s) = v(s)*D(s)$). Then, the time-domain response can be derived by calculating the inverse Laplace transform of $v'(s)$, which results in (5.12) when $\omega'$ was tuned to $\omega$. Compared with the ideal response in (5.10), (5.12) has the same steady-state term but a different exponential-attenuation term. Specifically, when $k$ is much smaller than $\omega'$, (5.12) can be simplified to (5.13) whose characteristic is close to (5.10) except for an additional exponential term which has much smaller value and will not influence the overall transient response so much. In this case, the dynamic response of the SOGI-QSG is close to that of the FOS, which explains the simulation result in Figure 5-18(a) where the settling time is designed to be 0.2 s.

$$\begin{aligned} v'(t) = {} & A\sin\left(\omega t+\varphi\right) + A\frac{\sin\left(t\sqrt{\omega'^2-k^2}\right)\left(-\omega'\cos\varphi + k\sin\varphi\right)}{\sqrt{\omega'^2-k^2}}e^{-tk} - \\ & A\sin\varphi\cos\left(t\sqrt{\omega'^2-k^2}\right)e^{-tk},\ t\ge 0 \end{aligned} \tag{5.12}$$

$$v'(t) \approx A\sin\left(\omega' t+\varphi\right) - A\sin\left(\omega' t+\varphi\right)e^{-kt} + A\frac{k\sin\left(\omega' t\right)\sin\varphi}{\omega'}e^{-kt},\ t\ge 0 \tag{5.13}$$

The second case has a much smaller settling time of 0.005s and the simulation result is given in Figure 5-18(b), where an obvious tracking error 15.46 % is produced by the SOGI-QSG at 0.005 s. However, the error is only 1.83 % for both the FOS and the ideal system in (5.10). Therefore, the design rule cannot be used anymore for the target SOGI-QSG system with a very fast dynamic response.

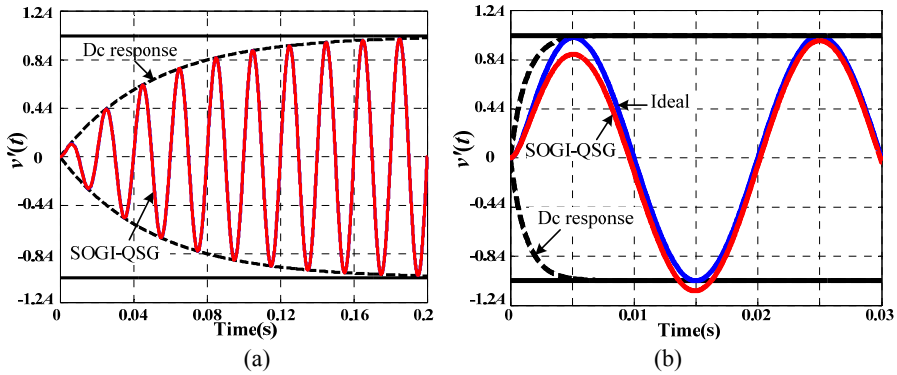


*Figure 5-18 Responses of SOGI-QSG to a sinusoidal input signal with different settling times (a) 0.2 s and (b) 0.005 s.*

## 5.3.2. PRINCIPLE OF THE PROPOSED AMI-QSG

It can be observed from (5.12) that the transient response of SOGI-QSG is highly nonlinear which makes its parameter design difficult. One solution to this problem is to find a sinusoidal integrator which when used to build a closed-loop system can lead to the same magnitude response with that of the FOS. Clearly, the complex integrator is one of the candidates, but its corresponding system needs a complex input signal which is difficult to obtain in a single-phase system. To solve the problem, an alternative integrator is presented in the follows, which is derived reversely from the ideal response (5.10) and is then used to build a QSG which has a much closer magnitude response to the FOS than SOGI-QSG.

### 5.3.2.1 Derivation of the accurate magnitude integrator

To start with, for a sinusoidal signal $v(t) = A\sin(\omega t+\varphi)$, its Laplace transform is:

$$v(s) = \frac{A\omega\cos\varphi}{s^2+\omega^2} + \frac{As\sin\varphi}{s^2+\omega^2}. \tag{5.14}$$

The ideal magnitude response has been given by (5.10) whose Laplace transform is:

$$v'(s) = \frac{A\omega\cos\varphi}{s^2+\omega^2} + \frac{As\sin\varphi}{s^2+\omega^2} - \frac{Ak(\cos\varphi+\sin\varphi)+As\sin\varphi}{(s+k)^2+\omega^2}. \tag{5.15}$$

With the above two transfer functions of the input and output signals, the closed-loop transfer function of the tracking system can be derived and then the open-loop transfer function can be calculated as:

$$O(s)=\frac{ks}{s^2+\omega^2}+\frac{k\omega}{s^2+\omega^2}\frac{-\omega\sin\varphi+(s+k)\cos\varphi}{\omega\cos\varphi+(s+k)\sin\varphi}. \tag{5.16}$$

Finally, (5.16) is the transfer function of the ideal sinusoidal integrator which ensures that the magnitude response of its corresponding tracking system is the same with that of the FOS. Unfortunately, it is noted that the transfer function $O(s)$ is related to the initial phase of the input signal, which is not easy to obtain in practice and thus complicates the implementation. Herein, assuming a special case when the phase $\varphi$ is zero, (5.16) can then be simplified as:

$$O'(s)=\frac{2ks+k^2}{s^2+\omega^2} \tag{5.17}$$

Similar to the GI, (5.17) is only related to the signal frequency and the time constant, which is thus easier to implement than (5.16). Considering that (5.17) is derived from a special case, its effectiveness should be validated for the general cases. To do it, the transfer function of the closed-loop system built by (5.16) is first given by:

$$D'(s)=\frac{2ks+k^2}{s^2+2ks+k^2+\omega^2} \tag{5.18}$$

Considering again $v=A\sin(\omega t+\varphi)$ as the input signal of the system, the response can be derived as :

$$v'(t)=A\sin(\omega t+\varphi)-A\sin(\omega t+\varphi)e^{-kt}+A\frac{k\sin(\omega t)\sin\varphi}{\omega}e^{-kt} \tag{5.19}$$

It is interesting to note that (5.19) is actually the same as (5.13). However, different from (5.13) which can only be satisfied when the settling time is small enough, (5.19) is always true regardless of the system parameters. The settling time of the corresponding system can therefore be designed more accurately.

### 5.3.2.2 Structure realization of the AMI based QSG

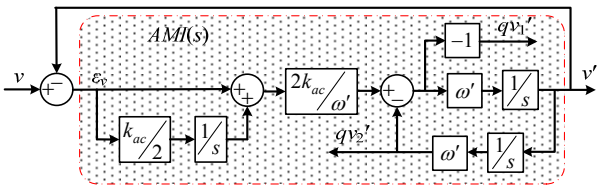


*Figure 5-19 Structure of the Accurate-MI based QSG (AMI-QSG).*

To implement the QSG with the proposed AMI, (5.17) is rewritten as

$$AMI(s)=\frac{2ks+k^2}{s^2+\omega'^2}=\frac{2k}{\omega'}\left(1+\frac{k}{2s}\right)\frac{\omega'/s}{1+\omega'^2/s^2} \tag{5.20}$$

The right-side term of (5.20) can be looked as the closed-loop transfer function of a system which has a gain $\omega'/s$ in both its feedback path and the forward path. Thus, its block diagram can easily be obtained as shown in Figure 5-19. To understand the principle of the AMI-QSG, transfer functions for relating $v'$ to $v$, $\varepsilon_v$ to $v$, $qv_1'$ to $v$, and $qv_2'$ to $v$ can be given by (5.18) and (5.21) - (5.23) respectively. Their Bode diagrams are plotted in Figure 5-20. It can be concluded that, at $\omega'$, $v'$ is the low-pass-filtered version of the input with no phase shift, $\varepsilon_v$ is the notch-filtered version of the input, $qv_1'$ is the high-pass-filtered version of the input with 90° of phase shift, and $qv_2'$ is the integral-filtered version of the input with 90° of phase shift. The integral characteristic of $Q_2(s)$ will have the dc drift problem like the pure integrator. Therefore, $qv_1'$ is finally used as the quadrature output of the proposed AMI-QSG.

$$E(s)=\frac{v(s)-v'(s)}{v(s)}=\frac{s^2+\omega'^2}{s^2+2ks+k^2+\omega^2} \tag{5.21}$$

$$Q_1(s)=\frac{qv_1'(s)}{v(s)}=-\frac{1}{\omega'}\frac{2ks^2+k^2s}{s^2+2ks+k^2+\omega^2} \tag{5.22}$$

$$Q_2(s)=\frac{qv_2'(s)}{v(s)}=\frac{\omega'}{s}\frac{2ks+k^2}{s^2+2ks+k^2+\omega^2} \tag{5.23}$$

In practice, the measured signal contains a dc component, which may be produced in the A/D process or when a fault occurs. Due to the low-pass characteristic of $D(s)$, the dc component will be transferred to the output $v'$ and introduce errors in the estimated results. Even worse, the dc component can cause the integrator before the output $qv_2'$ into saturation. If the integrator is saturated, the overall QSG algorithm will fail to work. Therefore, it is necessary to add an extra integrator as shown in Figure 5-21 to extract the input dc component. Detailed experimental validation can be found in **C5**.

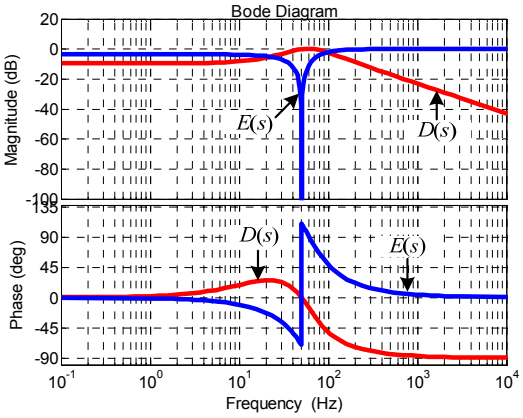


(a)

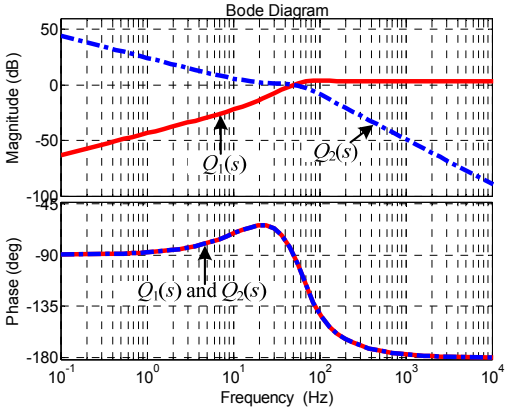


(b)

*Figure 5-20 Bode diagrams of AMI-QSG, (a) E(s) and D(s), (b) $Q_1(s)$ and $Q_2(s)$.*

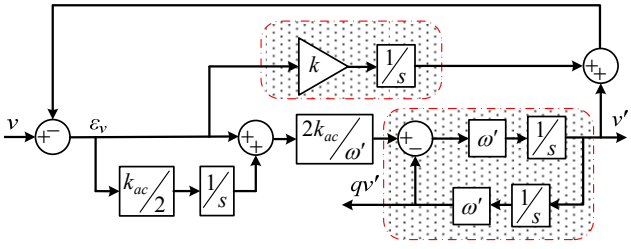


*Figure 5-21 Structure realization of the AMI-QSG with dc rejection.*

## 5.4. SUMMARY

This chapter presents two approaches to re-investigate the SOGI-QSG based filters, which are from the FOS perspective and the circuit perspective respectively. With these two approaches, the principle of the SOGI-based filters can be intuitively understood. Further, two advanced SOGI-QSGs are proposed and their effectiveness is validated by simulation and/or experimental results.

# CHAPTER 6. SUMMARY AND CONCLUSIONS

## 6.1. SUMMARY AND ACHIEVEMENTS

To cope with the stability and the power quality issues of the LCL-filtered VSI and to enhance its performance in case of abnormal grid conditions, this thesis has proposed a series of solutions which advances the systems, including: two advanced digital differentiators for active damping control, stability enhancement strategy for the grid-current control system, harmonic control strategy for the inverter-current control system, and improved QSGs for grid synchronization.

Specifically, the non-ideal GI differentiator has an adjustable characteristic and it alleviates the noise-amplification and phase-error issues of the typical differentiators. On the other hand, the SOGI-based differentiator has a fixed characteristic, while it contributes to the time-delay compensation which can enhance the stability of the control system. With these two schemes, active damping can be implemented cost-effectively.

A robust active damping gain is derived, which fixes the stable region of the dual-loop GCF scheme below the critical frequency regardless of the variation of the LCL-filter parameters and the grid impedance. A time-delay compensation technique is further proposed to widen the stable region of the dual-loop GCF control system, which highly improves the robustness of the control system against LCL-filter parameters and grid-impedance variations.

The findings obtained in the former two contributions help to develop an advanced harmonic control scheme for the ICF-controlled VSI. Different from the traditional methods, the developed method applies harmonic controllers and the feedforward scheme simultaneously, and the instability risk introduced by the feedforward loop can be ingeniously avoided through a special selection of the feedforward position, which maintains the inherent stability characteristic of the ICF control system. Besides, parameters of the proposed control system can be designed conveniently by referring to that of the typical single-loop ICF control system.

Finally, a comprehensive review of the SOGI-based filters is provided from a first-order system and a circuit perspective, based on which, an improved SO-SOGI-QSG is proposed. The proposed method inherits the simplicity of the basic SOGI-QSG and at the same time, it has an enhanced filtering performance. The proposed method is more appropriate for adverse grid conditions.

## 6.2. CONCLUSIONS

The high penetration of power converters used for the renewable energy generation systems imposes new challenges to the power quality and the stability of the power system. This thesis focuses on the performance improvement of the gird-connected LCL-filtered VSI system and has developed a series of strategies to optimize the control system implementation, enhance the system stability, and improve the power quality. Specifically, the non-ideal GI differentiator ensures accurate implementation of the active damping control in a digital control system. Besides, the SOGI-based time-delay compensation technique extends the stable region of the control system and hence enhances the system stability. Further, the proposed harmonic control strategy makes the ICF-controlled system be able to mitigate the grid-side current harmonics. Finally, the proposed SO-SOGI-FLL has enhanced harmonic attenuation performance, which is able to provide accurate grid synchronization even under distorted grid condition. In conclusion, the strategies developed in this thesis contribute to the improvement of the stability and power quality of the renewable energy generation systems, which are expected to promote a further increase of the contribution of the renewable energies to the global electricity demand.

## 6.3. FUTURE WORK

The achievements of this thesis also open opportunities for further development and research. Several issues of high interest for future research are listed as follows:

**(1) Influence of the *dq*-frame decoupling term on the system stability**

The control system can also be implemented in the synchronous frame. However, different from the stationary frame, a cross-coupling term exists between the *d*-axis and *q*-axis currents in the synchronous frame, which needs to be decoupled to ensure a high-performance operation. On the other hand, the influence of the decoupling term on the system stability is unknown, which should be investigated based on a precise modeling of the control system in *dq*-frame.

**(2) Systematical design of the current control system considering the control performance and the system stability simultaneously**

The critical damping gains for the ICF and GCF schemes have been derived in recent research, which can ensure the system stability regardless of the location of the LCL-filter resonance. However, the condition of this gain is very strict, since it requires the system to obtain passivity, which may limit the control performance of the system. Systematical design of the dual-loop current control system considering both the system stability and the control performance needs to be researched.

**(3) Optimized LCL-filter design considering the grid impedance variation and grid-voltage distortion**

The typical design of LCL-filter mainly considers the switching-ripple attenuation, volume, cost, efficiency, etc., which often leads to a small grid-side inductance. As a result, the resonance frequency will be sensitive to the grid impedance variation and may cause instability. Besides, compared with the L filter, the total inductance of the LCL-filter is very small due to its strong attenuation performance, which, on the other hand, limits its attenuation performance to the low-order harmonics and makes it sensitive to the grid-voltage distortion. Optimized LCL-filter design considering these requirements should be investigated.

**(4) Stability analysis of the control system taking account of the outer loops**

Apart from the inner current control loop, the outer loops (such as the voltage control loop, phase-locked loop, and power control loop) also influence the response and the stability characteristics of the control system. Modeling and analysis of the control system considering the outer loops is also worth to investigate.

**(5) Advanced control techniques**

The PI (or PR) controller was the most widely used technique for power converter applications. Despite its wide applications, it has some fundamental limitations. For instance, the integral term, though critical to eliminate the stead-state error, introduces saturation risk and reduces the stability margin of the system due to its phase lag. To increase the performance and stability of the power converter control system, it is necessary to seek and research alternative control techniques for the power converter systems. The active disturbance rejection control, which believes to be a capable replacement of PI control in control fields, is a promising candidate.

**(6) Accurate modeling and stability analysis of the VSI system considering the deadtime effect, the modulation schemes, and the saturation of the inductors**

Previous modeling has mainly concentrated on ideal systems, which ignores some non-linear factors such as the dead-time effect, the modulation schemes, and the saturation of the inductors. The shaping effects of these factors on the impedance of the VSI system are still unknown, which may introduce inaccuracy to the stability analysis. It is thus of great importance to explore more accurate models of the VSI system including these non-linear factors.

# LITERATURE LIST


[1] ExxonMobil, “2017 outlook for energy: a view to 2040” [Online]. Available: http://cdn.exxonmobil.com/~/media/global/files/outlook-for-energy/2017/2017_outlook_for_energy.pdf.

[2] ExxonMobil, “2016 outlook for energy: a view to 2040” [Online]. Available: http://cdn.exxonmobil.com/~/media/global/files/outlook-for-energy/2016/2016-outlook-for-energy.pdf.

[3] X. Wang, F. Blaabjerg, and W. Wu, “Modeling and analysis of harmonic stability in an AC power-electronics-based power system,” *IEEE Trans. Power Electron*., vol. 29, no. 12, pp. 6421–6432, Dec. 2014.

[4] X. Wang, Y. W. Li, F. Blaabjery, and P. Chiang Loh, “Virtualimpedance-based control for voltage-source and current-source converters,” *IEEE Trans. Power Electron*., vol. 30, no. 12, pp. 7019–7037, Dec. 2015.

[5] F. Blaabjerg, R. Teodorescu, M. Liserre, and A. V. Timbus, “Overview of control and grid synchronization for distributed power generation systems,” *IEEE Trans. Ind. Electron*., vol. 53, no. 5, pp. 1398–1409, Oct. 2006.

[6] Z. Wang and L. Chang, “A DC voltage monitoring and control method for three-phase grid connected wind turbine inverters,” *IEEE Trans. Power Electron*., vol. 23, no. 3, pp. 1118–1125, May 2008.

[7] N. Pogaku, M. Prodanovic, and T. C. Green, “Modeling, analysis and testing of autonomous operation of an inverter-based microgrid,” *IEEE Trans. Power Electron*., vol. 22, no. 2, pp. 613–625, Mar. 2007.

[8] Y. Wang, Z. Chen, X. Wang, Y. Tian, Y. Tan, and C. Yang, “An estimator-based distributed voltage-predictive control strategy for AC islanded microgrids,” *IEEE Trans. Power Electron*., vol. 30, no. 7, pp. 3934–3951, Mar. 2015.

[9] M. Liserre, F. Blaabjerg, and S. Hansen, “Design and control of an LCL- filter based three-phase active rectifier,” *IEEE Trans. Ind. Appl*., vol. 41, no. 5, pp. 1281–1291, Sep./Oct. 2005.

[10] D. Pan, X. Ruan, C. Bao, W. Li, and X. Wang, “Optimized controller design for LCL-type grid-connected inverter to achieve high robustness against grid-impedance variation,” *IEEE Trans. Ind. Electron*., vol. 62, no. 3, pp. 1537–1547, Mar. 2015.

[11] Y. Tang, W. Yao, P. C. Loh, and F. Blaabjerg, “Design of LCL-filters with LCL resonance frequencies beyond the Nyquist frequency for grid-connected converters,” *IEEE J. Emerg. Sel. Topics Power Electron*., vol. 4, no. 1, pp. 3–14, Jul. 2015.

[12] A. A. Rockhill, M. Liserre, R. Teodorescu, and P. Rodriguez, “Grid-filter design for a multimegawatt medium-voltage voltage-source inverter,” *IEEE Trans. Ind. Electron*., vol. 58, no. 4, pp. 1205–1217, Apr. 2011.

[13] T. Wang, Z. Ye, G. Sinha, and X. Yuan, “Output filter design for a grid-interconnected three-phase inverter,” in *Proc. IEEE PESC*, 2003, vol. 2, pp. 779–784.

[14] A. K. Sahoo, A. Shahani, K. Basu, and N. Mohan, “LCL filter design for grid-connected inverters by analytical estimation of PWM ripple voltage,” in *Proc. IEEE APEC*, 2014, pp. 1281–1286.

[15] R. Pena-Alzola, M. Liserre, F. Blaabjerg, R. Sebastian, J. Dannehl, and F. W. Fuchs, "Analysis of the passive damping losses in LCL-filter-based grid converters," *IEEE Trans. Power Electron*., vol. 28, no. 6, pp. 2642–2646, Jun. 2013.

[16] P. Channegowda and V. John, "Filter optimization for grid interactive voltage source inverters," *IEEE Trans. Ind. Electron*., vol. 57, no. 12, pp. 4106–4144, Dec. 2010.

[17] V. Blasko and V. Kaura, "A novel control to actively damp resonance in input LC filter of a three-phase voltage source converter," *IEEE Trans. Ind. Appl*., vol. 33, no. 2, pp. 542–550, Mar. 1997.

[18] D. Pan, X. Ruan, C. Bao, W. Li, and X. Wang, "Capacitor-current-feedback active damping with reduced computation delay for improving robustness of LCL-type grid-connected inverter," *IEEE Trans. Power Electron*., vol. 29, no. 7, pp. 3414–3427, Jul. 2014.

[19] R. Pena-Alzola, M. Liserre, F. Blaabjerg, R. Sebastian, J. Dannehl, and F. W. Fuchs, "Systematic design of the lead-lag network method for active damping in LCL-filter based three phase converters," *IEEE Trans. Ind. Inf*., vol. 10, no. 1, pp. 43–52, Feb. 2014.

[20] X. Li, X. W, Y. Geng, X. Yuan, C. Xia, and X. Zhang, "Wide damping region for LCL-type grid-connected inverter with an improved capacitor-current-feedback method," *IEEE Trans. Power Electron*., vol. 30, no. 9, pp. 5247–5259, Sep. 2015.

[21] X. Wang, F. Blaabjerg, and P. C. Loh, "Virtual RC damping of LCL-filtered voltage source converters with extended selective harmonic compensation," *IEEE Trans. Power Electron*., vol. 30, no. 9, pp. 4726–4737, Sep. 2015.

[22] J. Dannehl, F. W. Fuchs, S. Hansen, and P. B. Thogersen, "Investigation of active damping approaches for PI-based current control of grid-connected pulse width modulation converters with LCL filters," *IEEE Trans. Ind. Appl*., vol. 46, no. 4, pp. 1509–1517, Jul. –Aug. 2010.

[23] J. Xu, S. Xie, and T. Tang, "Active damping-based control for grid-connected LCL-filtered inverter with injected grid current feedback only," *IEEE Trans. Ind. Electron*., vol. 61, no. 9, pp. 4746–4758, Sep. 2014.

[24] X. Wang, F. Blaabjerg, and P. C. Loh, "Analysis and design of grid-current-feedback active damping for LCL resonance in grid-connected voltage source converters," in *Proc. of IEEE ECCE*, 2014, pp. 373–380.

[25] IEEE Standard for Interconnecting Distributed Resources With Electric Power Systems, IEEE Std. 1547-2003, Jul. 28, 2003.

[26] X. Zong, P. A. Gray, and P. W. Lehn, "New metric recommended for IEEE Standard 1547 to limit harmonics injected into distorted grids," *IEEE Trans. Power Deliv*., vol. 31, no. 3, pp. 963–972, Jun. 2016.

[27] T. Abeyasekera, C. M. Johnson, D. J. Atkinson, and M. Armstrong, "Suppression of line voltage related distortion in current controlled grid connected inverters," *IEEE Trans. Power Electron*., vol. 20, no. 6, pp. 1393– 1401, Nov. 2005.

[28] Y. Yang, K. Zhou, H. Wang, F. Blaabjerg, D. Wang, and B. Zhang, "Frequency adaptive selective harmonic control for grid-connected inverters," *IEEE Trans. Power Electron*., vol. 30, no. 7, pp. 3912–3924, Jul. 2015.

[29] W. Li, X. Ruan, D. Pan, and X. Wang, "Full-feedforward schemes of grid voltages for a three-phase LCL-type grid-connected inverter," *IEEE Trans. Ind. Electron*., vol. 60, no. 6, pp. 2237–2250, Jun. 2013.

[30] Q. Yan, X. Wu, X. Yuan, and Y. Geng, "An improved grid-voltage feedforward strategy for high-power three-phase grid-connected inverters based on the simplified repetitive predictor," *IEEE Trans. Power Electron*., vol. 31, no. 5, pp. 3880-3897, May 2016.

[31] R. Teodorescu, M. Liserre, and P. Rodriguez, *Grid converters for photovoltaic and wind power systems*. Hoboken, NJ, USA: Wiley, 2011.

[32] M. Ciobotaru, R. Teodorescu, and F. Blaabjerg, "A new single-phase PLL structure based on second order generalized integrator," in *Proc. IEEE PESC'06*, Jun. 2006, pp. 1–6.

[33] P. Rodriguez, A. Luna, R.S. Munoz-Aguilar, I. Etxeberria-Otadui, R. Teodorescu, F. Blaabjerg, "A stationary reference frame grid synchronization system for three-phase grid-connected power converters under adverse grid conditions," *IEEE Trans. Power Electron*., vol. 27, no. 1, pp. 99–112, Jan. 2012.

[34] J. Matas, M. Castilla, J. Miret, L. García de Vicuña, and R. Guzman, "An adaptive pre-filtering method to improve the speed/accuracy trade-off of voltage sequence detection methods under adverse grid conditions," *IEEE Trans. Ind. Electron*., vol. 61, no. 5, pp. 2139–2151, May 2014.

[35] M. Karimi-Ghartemani, S. Khajehoddin, P. Jain, A. Bakhshai, and M. Mojiri, "Addressing DC component in PLL and notch filter algorithms," *IEEE Trans. Power Electron*., vol. 27, no. 1, pp. 78–86, Jan. 2012.

[36] J. Wang, J. D. Yan, L. Jiang and J. Zou, "Delay-dependent stability of single-loop controlled grid-connected inverters with LCL filters," *IEEE Trans. Power Electron*., vol. 31, no. 1, pp. 743–757, Jan. 2016.

[37] Z. Xin, X. Wang, P. C. Loh, and F. Blaabjerg, "Grid-current-feedback control for LCL-filtered grid converters with enhanced stability," *IEEE Trans. Power Electron*., vol. 32, no. 4, pp. 3216–3228, Apr. 2017.

[38] C. Zou, B. Liu, S. Duan, and R. Li, "Influence of delay on system stability and delay optimization of grid-connected inverters with LCL filter," *IEEE Trans. Ind. Inform*., vol. 10, no. 3, pp. 1775-1784, Aug. 2014.

[39] S. G. Parker, B. P. McGrath, and D. G. Holmes, "Regions of Active Damping Control for LCL Filters," *IEEE Trans. Ind. Appl*., vol. 50, pp. 424-432, Jan/Feb. 2014.

[40] R. Peña Alzola, M. Liserre, F. Blaabjerg, M. Ordonez, and T. Kerekes, "A self-commissioning notch filter for active damping in a three-phase LCL -filter-based grid-tie converter," *IEEE Trans. Power Electron*., vol. 29, no. 12, pp. 6754–6761, Dec. 2014.

[41] Z. Xin, P. C. Loh, X. Wang, F. Blaabjerg, and Y. Tang, "Highly accurate derivatives for LCL-Filtered grid converter with capacitor voltage active damping," *IEEE Trans. Power Electron*., vol. 31, no. 5, pp. 3612–3625, May 2016.

[42] A. G. Yepes, F. D. Freijedo, J. Doval-Gandoy, O. Lopez, J. Malvar, and P. Fernandez-Comesana, "Effects of discretization methods on the per-formance of resonant controllers," *IEEE Trans. Power Electron*., vol. 25, no. 7, pp. 1692–1712, Jul. 2010.

[43] S. Bibian and H. Jin, "Time delay compensation of digital control for DC switchmode power supplies using prediction techniques," *IEEE Trans. Power Electron*., vol. 15, no. 5, pp. 835–842, Sep. 2000.

[44] V. Miskovic, V. Blasko, T. Jahns, A. Smith, and C. Romenesko, "Observer based active damping of LCL resonance in grid connected voltage source converters," *IEEE Trans. Ind. Appl*., vol. 50, no. 6, pp. 3977–3985, Nov./Dec. 2012.

[45] S. Y. Park, C. L. Chen, J. S. Lai, and S. R. Moon, "Admittance compen- sation in current loop control for a grid-tie LCL fuel cell inverter," *IEEE Trans. Power Electron*., vol. 23, no. 4, pp. 1716–1723, Jul. 2008.

[46] T.-F. Wu, L.-C. Lin, N. Yao, Y.-K. Chen, and Y.-C. Chang, "Extended application of D-Σ digital control to single-phase bi-directional inverter with LCL filter," *IEEE Trans. Power Electron*., vol. 30, no. 7, pp. 3903– 3911, Jul. 2015.

[47] Y. Tang, P. C. Loh, P. Wang, F. H. Choo, and F. Gao, "Exploring inherent damping characteristic of LCL-filters for three-phase grid-connected voltage source inverters," *IEEE Trans. Power Electron*., vol. 27, no. 3, pp. 1433–1443, Mar. 2012.

[48] G. Escobar, M. J. Lopez-Sanchez, and J. M. Sosa, "Inverter-side current control of a single-phase inverter grid connected trough an LCL filter," in *Proc. 40th IEEE IECON*., Oct. 2014, pp. 5552–5558.

[49] W. Yao, X. Wang, P. C. Loh, X. Zhang, and F. Blaabjerg, "Improved power decoupling scheme for a single-phase grid-connected differential inverter with realistic mismatch in storage capacitances," *IEEE Trans. Power Electron*., vol. 32, no. 1, pp. 186– 199, Jan. 2017.

[50] Z. Zeng, B. Hu, H. Li, L. Ran, W. Shao, and W. Zhao, "Analysis on controller of grid-connected inverter by using virtual circuit," *EPE'15- ECCE, European Conf. on Power Electron. & Appl*., pp. 1-8, 2015.

[51] D. G. Holmes, T. A. Lipo, B. P. McGrath, and W. Y. Kong, "Optimized design of stationary frame three-phase ac current regulators," *IEEE Trans. Power Electron*., vol. 24, no. 11, pp. 2417–2426, Nov. 2009.

[52] Z. Xin, X. Wang, P. C. Loh, and F. Blaabjerg, "Realization of digital differentiator using generalized integrator for power converters," *IEEE Trans. Power Electron*., vol. 30, no. 12, pp. 6520–6523, Dec. 2015.

[53] Burger, B. und A. Engler, " Verfahren und Vorrichtung zur Bestimmung charakteristischer Größen aus einem zeitlich periodischem Signal," German Patent 199 49 997.7, Oct. 15, 1999.

[54] B. Burger and A. Engler, "Fast signal conditioning in single phase systems," in *Proc. Eur. Conf. Power Elect. Appl*., 2001, pp. 1–10.

[55] R. I. Bojoi, G. Griva, M. Guerriero, F. Farina, F. Profumo, and V. Bostan, "Improved current control strategy for power conditioners using sinusoidal signal integrators in synchronous reference frame," in *Proc. IEEE 35th Annu. Power Electron. Spec. Conf*., 2004, pp. 4623–4629.

[56] R. I. Bojoi, G. Griva, V. Bostan, M. Guerriero, F. Farina, and F. Profumo, "Current control strategy for power conditioners using sinusoidal signal integrators in synchronous reference frame," *IEEE Trans. Power Electron*., vol. 20, no. 6, pp. 1402–1412, Nov. 2005.

[57] P. Rodriguez, A. Luna, M. Ciobotaru, R. Teodorescu, and F. Blaabjerg, "Advanced grid synchronization system for power converters under unbalanced and distorted operating conditions," in *Proc. 32nd IEEE IECON*, 2006, pp. 5173–5178.

[58] M. Mojiri and A. Bakhshai, "An adaptive notch filter for frequency estimation of a periodic signal," *IEEE Trans. Autom. Control*, vol. 49, no. 2, pp. 314–318, Feb. 2004.

[59] P. A. Regalia, "An improved lattice-based adaptive IIR notch filter," *IEEE Trans. Signal Process*., vol. 39, no. 9, pp. 2124–2128, Sep. 1991.

[60] M. Bodson and S. C. Douglas, "Adaptive algorithms for the rejection of sinusoidal disturbances with unknown frequency," *Automatica*, vol. 33, no. 12, pp. 2213–2221, Dec. 1997.

[61] L. Hsu, R. Ortega, and G. Damm, "A globally convergent frequency estimator," *IEEE Trans. Autom. Control*, vol. 44, no. 4, pp. 698–713, Apr. 1999.

[62] P. Rodriguez, A. Luna, I. Candela, R. Teodorescu, and F. Blaabjerg, "Grid synchronization of power converters using multiple second order generalized integrators," in *Proc. 34th IEEE IECON*., 2008, pp. 755–760.

[63] P. Rodriguez, A. Luna, I. Etxeberria, J. R. Hermoso, and R. Teodorescu, "Multiple second order generalized integrators for harmonic synchronization of power converters," in *Proc. IEEE Energy Convers. Congr. Expo*., 2009, pp. 2239–2246.

[64] P. Rodriguez, A. Luna, I. Candela, R. Mujal, R. Teodorescu, and F. Blaabjerg, "Multiresonant frequency-locked loop for grid synchronization of power converters under distorted grid conditions," *IEEE Trans. Ind. Electron*., vol. 58, no. 1, pp. 127–138, Jan. 2011.

[65] M. Mojiri, M. Karimi-Ghartemani, and A. Bakhshai, "Time-domain signal analysis using adaptive notch filter," *IEEE Trans. Signal Process*., vol. 55, no. 1, pp. 85–93, Jan. 2007.

[66] M. Mojiri and A. Bakhshai, "Estimation of n frequencies using adaptive notch filter," *IEEE Trans. Circuits Syst. II, Exp. Briefs*, vol. 54, no. 4, pp. 338–342, Apr. 2007.

[67] D. Yazdani, M. Mojiri, A. Bakhshai, and G. Joos, "A fast and accurate synchronization technique for extraction of symmetrical components," *IEEE Trans. Power Electron*., vol. 24, no. 3, pp. 674–684, Mar. 2009.

[68] J. Matas, M. Castilla, L. G. de Vicuña, J. Miret, and J. C. Vasquez, "Virtual impedance loop for droop-controlled single-phase parallel inverters using a second-order general-integrator scheme," *IEEE Trans. Power Electron*., vol. 25, no. 12, pp. 2993–3002, Dec. 2010.

[69] G. Wang, L. Ding, Z. Li, J. Xu, G. Zhang, H. Zhan, R. Ni, and D. Xu, "Enhanced position observer using second-order generalized integrator for sensorless interior permanent magnet synchronous motor drives," *IEEE Trans. Energy Convers*., vol. 29, no. 2, pp. 486–495, Jun. 2014.

[70] J. A. Suul, A. Luna, P. Rodriguez, and T. Undeland, "Virtual-flux-based voltage-sensor-less power control for unbalanced grid conditions," *IEEE Trans. Power Electron*., vol. 27, no. 9, pp. 4071–4087, Jul. 2012.

[71] R. W. C. G. R. Wijshoff, M. Mischi, and R. M. Aarts, "Reducing of periodic motion artifacts in photoplethysmograms," *IEEE Trans. Biomed. Eng*., 10.1109/TBME.2016.2553060.

[72] M. Ghadiri-Modarres, M. Mojiri, and M. Karimi-Ghartemani, "New adaptive algorithm for delay estimation of sinusoidal signals with unknown frequency," *IEEE Trans. Instrum. Meas*., vol. 64, no. 9, pp. 2360–2366, Sep. 2015.

[73] M. Mansouri, M. Mojiri, M. A. Ghadiri-Modarres, and M. Karimi-Ghartemani, "Estimation of electromechanical oscillations from phasor measurements using second-order generalized integrator," *IEEE Trans. Instrum. Meas*., vol. 64, no. 4, pp. 943–950, Apr. 2015.

[74] S. Hu, Automatic control theory, 6th ed. Beijing: Science Press, 2013.

[75] Z. Xin, R. Zhao, P. Mattavelli, P. C. Loh, and F. Blaabjerg, "Re-investigation of generalized integrator based filters from a first-order-system perspective," *IEEE Access*, vol. 4, pp. 7131–7144, Nov. 2016.

[76] X. Yuan, J. Allmeling, W. Merk, and H. Stemmler, "Stationary frame generalized integrators for current control of active power filters with zero steady state error for current harmonics of concern under unbalanced and distorted operation conditions," in *Conf. Rec. IEEE-IAS Annu. Meeting*, 2000, pp. 2143–2150.

[77] X. Guo, W. Wu, and Z. Chen, "Multiple-complex coefficient-filter-based phase-locked loop and synchronization technique for three-phase grid- interfaced converters in distributed utility networks," *IEEE Trans. Ind. Electron*., vol. 58, no. 4, pp. 1194–1204, Apr. 2011.

[78] X. Yuan, W. Merk, H. Stemmler, and J. Allmeling, "Stationary-frame generalized integrators for current control of active power filters with zero steady-state error for current harmonics of concern under unbalanced and distorted operating conditions," *IEEE Trans. Ind. Appl*., vol. 38, no. 2, pp. 523–532, Mar./Apr. 2002.

[79] W. Li, X. Ruan, C. Bao, D. Pan, and X. Wang, "Grid synchronization systems of three-phase grid-connected power converters: A complex vector-filter perspective," *IEEE Trans. Ind. Electron*., vol. 61, no. 4, pp. 1855–1870, Apr. 2014.

[80] Z. Xin, X. Wang, Z. Qin, M. Lu, P. C. Loh, and F. Blaabjerg, "An improved second-order generalized integrator based quadrature signal generator," *IEEE Trans. Power Electron*., vol. 31, no. 12, pp. 8068–8073, Dec. 2016.

[81] G. F. Franklin, J.D. Powell, and A. Emami-Naeini, *Feedback Control of Dynamic systems*, 6th ed. Englewood Cliffs, NJ: Prentice-Hall, 2009.

# APPENDICES

# Appendix A. Experimental parameters of Chapter 2

| System Parameters | | | |
|---|---|---|---|
| Grid frequency $f_0$ | 50 Hz | Grid inductance $L_g$ | 1.25 mH |
| Switching frequency $f_{sw}$ | 10 kHz | Sampling frequency $f_s$ | 10 kHz |
| **Parameters of the LCL Filter** | | | |
| Inverter-side inductance $L_1$ | 4.9 mH | Grid-side inductance $L_2$ | 1.8 mH |
| Filter capacitance $C$ | 5 μF | Resonance frequency $f_r$ | 2.26 kHz |

# Appendix B. Experimental parameters of Chapter 3

| System Parameters | | | |
|---|---|---|---|
| Grid frequency $f_0$ | 50 Hz | Grid inductance $L_g$ | 0 mH |
| Switching frequency $f_{sw}$ | 10 kHz | Sampling frequency $f_s$ | 10 kHz |
| **Parameters of the LCL Filter** | | | |
| Inverter-side inductance $L_1$ | 1.8 mH | Grid-side inductance $L_2$ | 1.25 mH |
| Filter capacitance $C$ | 10 μF | Resonance frequency $f_r$ | 1.85 kHz |

# Appendix C. Experimental parameters of Chapter 4

| System Parameters | | | |
|---|---|---|---|
| Output Power $P_o$ | 7.5 kW | Grid voltage $v_g$ | 220 Vrms |
| Grid frequency $f_0$ | 50 Hz | Grid inductance $L_g$ | 0 mH |
| Dc-link voltage $v_{dc}$ | 650 V | | |
| Switching frequency $f_{sw}$ | 20 kHz | Sampling frequency $f_s$ | 20 kHz |
| **Parameters of the LCL Filter** | | | |
| Inverter-side inductance $L_1$ | 1.1 mH | Grid-side inductance $L_2$ | 1.1 mH |
| Filter capacitance $C$ | 20 μF | | |

ISSN (online): 2446-1636
ISBN (online): 978-87-7112-927-4

AALBORG UNIVERSITY PRESS